AN ABSTRACT OF THE THESIS OF

Michael R. MacQuigg for the degree of Master of Science in Nuclear Engineering presented on July 26, 2011.
Title: Pair Production Treatments for Deterministic Pulse-Height Distribution Simulations

Abstract approved: _____
Todd S. Palmer

This thesis presents methods for treating annihilation photon pairs in deterministic pulse height distribution (PHD) simulations. The methods are applied in PHD simulations for monoenergtic sources of 1.6 and 2.6 MeV photons incident on 5 and 10 cm 1-D slabs of germanium, sodium iodide, and lead and the results are compared with PHD simulations generated using MCNP5. Comparisons show good agreement between the peak area estimates of the deterministic and Monte Carlo codes. Average relative error in peak area estimates compared to the MCNP5 benchmark was 7%. A new treatment for the distribution of energy deposition resulting from group-to-group transfer is introduced that provides limited improvement in resolution when compared to treatments used in previous work [1]. An iteration parameter study is also conducted on slab geometry systems composed of carbon, silicon, germanium, tin, lead, and lead sodium iodide of various thickness. The results indicate a maximum of approximately seven iterations required to converge transport solutions (>95% of escaping boundary current) for spatially uniform distributions of 0.511 MeV photons in 5 cm thick slabs.

Pair Production Treatments for Deterministic Pulse-Height Distribution Simulations

by

Michael R. MacQuigg

A THESIS

submitted to

Oregon State University

in partial fulfillment of
the requirements for the
degree of

Master of Science

Presented July 26, 2011
Commencement June, 2012

Master of Science thesis of Michael R. MacQuigg presented on July 26, 2011.

APPROVED:

Major Professor, representing Nuclear Engineering

Head of the Department of Nuclear Engineering and Radiation Health Physics

---

Dean of the Graduate School

I understand that my thesis will become part of the permanent collection of Oregon State University libraries. My signature below authorizes release of my thesis to any reader upon request.

Michael R. MacQuigg, Author

ACKNOWLEDGEMENTS

I would like to thank my advisor, Dr. Todd Palmer, for his tutelage and support throughout my stay at OSU. I would also like to extend my sincere gratitude to my friends and family. Without their help I would not be where I am today.

TABLE OF CONTENTS

TABLE OF CONTENTS (Continued)

Page

Page

LIST OF FIGURES

LIST OF TABLES

Pair Production Treatments for Deterministic Pulse-Height Distribution Simulations

1 Introduction

Many engineered systems are affected by radiation or depend on radiation by their design. Simulation of the interaction of radiation in complex geometries is therefore frequently a focus of study. Examples of applications which require this simulation include the development of satellites which require carefully designed shielding that protects delicate electronics from the constant bombardment of cosmic radiation. Such shielding must not only protect the satellite but also do so at a minimal weight. In other cases radiation is carefully administered for such things as radiation oncology where tumors are targeted to absorb doses lethal to the cancerous cells. In those procedures exposure to adjacent tissues and organs must be minimized. Other applications include radiation detection systems. Notable among detection systems are those capable of gathering spectral data used to examine the properties of a radiation source. Spectroscopic detectors are used in many ways including for the detection of radioactive contraband and in neutron activation analysis– the latter plays an important role in a diverse set of fields ranging from material testing to archeology.

These applications demonstrate the need for accurate analysis of radiation interactions with matter. But despite being well understood, predicting exactly how radiation will behave as it moves through all but the most simple of systems is impractical with hand calculations. Instead, researchers rely on digital computer simulations. Computers make it possible to complete and store the results of large numbers of calculations that are typically necessary for accurate estimates of radiation behavior.

Simulating the transport of radiation on digital computers is accomplished with numerical methods that fall into one of three categories: probabilistic (or *Monte Carlo*), deterministic and hybrid methods. Probabilistic methods recreate the behavior of individual particles by rigorously simulating their interactions and are capable of producing arbitrarily accurate results. However, tracking enough particles (histories) to garner results to a given level of accuracy can be prohibited by the amount of computation time required. This is generally the case in *optically thick* problems particles undergo a large number of interactions per unit distance.

Deterministic methods involve solutions of linear systems of equations which approximate the macroscopic behavior of radiation in a system. The solutions are therefore limited in accuracy by the equations used in the approximation. While bound by some limitations in accuracy, deterministic methods can be much faster, requiring only the number of calculations required to solve the system of equations to obtain an solution of maximum accuracy.

The newest set of methods, hybrid methods, combine elements of deterministic and Monte Carlo transport to give solutions more accurate that than those solved deterministically while converging faster than standard Monte Carlo simulations. This is accomplished by quickly obtaining a reduced resolution, reduced accuracy deterministic solution and using the result to guide biasing in a subsequent Monte Carlo (MC) simulation of the same problem. By biasing the distribution of MC histories, more particles (of lower weight) can be dedicated to improving the accuracy of results in regions of interest. Biasing is one approach to *variance-reduction*, a process that reduces the statistical error of a MC solution.

Ignoring computational requirements, all three classes of methods are capable of providing adequate simulations for a variety of transport problems. However,

the calculation of pulse height distributions has conventionally been performed with Monte Carlo methods. A pulse height distribution (PHD) is the probability distribution function of energy deposition events for particles incident on a detector volume. The energy deposited ranges between the particle's incident total energy and zero. Because PHDs are essentially based on the behavior of individual particles, Monte Carlo simulations have historically been thought of as the only logical approach for PHD calculations.

In 2008, Benz and Palmer [1] demonstrated a new method to calculate pulse height distributions using deterministic solutions of the transport equation. Using their method they were able to generate PHD estimates for 1-D models which closely matched results from the industry-standard MCNP5 Monte Carlo software package [1]. This approach did not specifically account for the effect of pair production interactions on the PHD. Pair production is a significant contributor to the PHD for systems with high atomic number constituents and incident photon energies exceeding 1.022 MeV.

The objective of this research is to develop and test new treatments of pair production within a deterministic transport calculation of the pulse height distribution. We will compare the effectiveness of these methods with the results previously calculated by Benz and Palmer, and with those from MCNP5. Metrics for comparison will include accuracy and computational efficiency.

1.1 Literature Review

Pulse height distribution simulation capabilities exist in current Monte Carlo software packages such as MCNP5 and the Integrated Tiger Series of MC transport codes[8][9]. The most prominent package, MCNP5, calculates pulse height distri-

butions by tallying the product of particle weight and energy. As a particle enters a cell (by crossing a surface or being born into the cell) a tally for the cell is credited by an amount equal to the product of the particle's weight and energy. If the particle escapes the cell, the product of the exiting weight and energy are removed from the tally and added to the tally of the adjacent cell. The energy used in these tallies is the particle's kinetic energy or, for positrons, the particle's kinetic energy plus a rest mass equivalency of 1.022 MeV. At the end of the particle's history the tallies are divided by the source weight– resulting in a value of deposited energy that can be sorted into arbitrarily chosen bins.

A distinction between MCNP5 and other codes is its treatment of uncollided particles and those from non-analog processes [9, p. 2-86]. MCNP5 uses a "zero bin" and an "epsilon bin." The zero bin provides a very small bin inside which very few energy deposition events occur– where uncollided particles can be tallied. This serves to separate counts of uncollided histories from histories that deposit a small but finite amount of energy into the adjacent epsilon bin.

In deterministic transport, PHD simulation has been demonstrated by Benz and Palmer [1]. Their method is explained in [1] and reviewed in Sections 1.8-1.8.3 of this thesis. Their approach is based on energy dependent current solutions at system boundaries. Components of flux introduced into a system in energy group g' that escape in energy group g are tracked and PHDs are created based on the magnitude of escaping components and, as is discussed in Section 2.8, the respective range of energy deposition resulting from $g' \rightarrow g$ energy group changes. Separation of uncollided flux from the PHD is accomplished as discussed in Section 2.8.

1.2 Radiation Interaction and Energy Deposition

The types of radiation of concern in the vast majority of applied radiation problems are gamma/X-ray (photon), beta (energetic electrons and positrons), and alpha (energetic helium nuclei). Photons originating from the decay of nuclei are generally known as gamma rays and X-rays refer to photons created through atomic orbital rearrangement or charge acceleration. However, there is no physical distinction between photons once they have been created and so in this thesis gamma will refer to photons of any source. Further, any type of radiation (beta, gamma, X-ray, photon) may be referred to as a particle.

As radiation travels through matter its interaction is a complex function of the properties of matter, and the energy, mass and charge of the radiation. The following sections explain the basic phenomena which govern the relevant radiation interactions with matter.

1.3 Interaction of Photon Radiation with Matter

A photon is quanta of energy carried in the form of an oscillating electromagnetic wave. These waves can be created in many ways but are commonly created at high energies (keV-MeV) during movement of electrons within atomic orbitals, during abrupt acceleration of charges, and during the decay of radioactive nuclei.

The interactions of photons with matter are driven solely by their interaction with the electric fields of atomic nuclei and atomic orbital electrons. The outcome of a photon's interaction with matter is therefore governed by photon energy and the charge density encountered by the photon as it traverses a material. In this thesis, three fundamental interactions are considered: photoelectric absorption,

Compton scattering, and pair production. A fourth interaction, coherent scattering, is ignored here because it is not of consequence in problems of interest to radiation detection and instrumentation[3].

1.3.1 Photoelectric Absorption

At small photon energy-to-atomic number ratios, photoelectric (PE) absorption is the prominent mode of interaction. A photon may undergo PE absorption only when its energy exceeds discrete potential energy values which bind atomic electrons in orbitals. When this condition is met, photons may be completely absorbed and an orbital electron emitted. Such electrons are known as a *photoelectrons* and will carry kinetic energy (E_{e^-}) equivalent to the difference between the photon energy ($h\nu$) and the binding energy (E_b) that was overcome to free the electron:

$$E_{e^-} = hv - E_b. \tag{1}$$

The kinetic energy of photoelectrons is limited by the tendency of atoms to emit electrons from orbitals of progressively higher binding energy, which results in higher losses of energy to overcoming the potential barrier[3]. Because the energy of photoelectrons is limited, so too are their range. Details on the range of energetic electrons is discussed later.

The vacancy left in atomic orbitals through photoelectric ionization is filled by the capture of an electron from the medium or from a higher-energy orbital. The latter results in the emission of a photon with energy equivalent to the difference in energy states between the two orbitals [3]. Such photons are known as characteristic X-rays (or fluorescent X-rays).

1.3.2 Compton Scattering

At intermediate photon energies, photoelectric absorption is much less probable. A nearly elastic collision process known as *Compton scattering* is the dominant mechanism in this energy range. Incident photons collide with an orbital electron and the photon and electron both emerge from the collision with new energies and directions. The electron is considered to be at rest and, though the interaction is ionizing, the binding energy is ignored because it has a minimal impact on the collision kinematics except at low energies [3]. The solution of simultaneous conservation equations of energy and momentum predicts the energy and direction distribution of Compton-scattered photons. The energy of a photon following a deflection through the angle θ in a Compton scatter is given by

$$h\nu = \frac{h\nu'}{1 + \frac{h\nu'}{m_0c^2}(1 - \cos(\theta))}. \tag{2}$$

The angular distribution of photons emerging from a Compton scattering event is predicted by the Klein-Nishina differential cross section:

$$\frac{d\sigma}{d\Omega} = Zr_0^2\left(\frac{1}{1+\alpha(1-\cos\theta)}\right)^2\left(\frac{1+\cos^2\theta}{2}\right)\times \left(1+\frac{\alpha^2(1-\cos\theta)^2}{(1+\cos^2\theta)[1+\alpha(1-\cos\theta)]}\right). \tag{3}$$

where

Z $\equiv$ electron density

$r_0 \equiv$ classical electron radius

$\alpha \equiv \frac{h\nu}{m_0c^2}$

1.3.3 Pair Production

At energies greater than or equal to 1.022 MeV, it is possible for photons to be converted into matter in the form of an electron-positron pair. A photon energy threshold of 1.022 MeV exists, which is the minimum energy needed to create the rest mass of an electron-positron pair. Pair production occurs when a photon interacts with a strong electric field such as those found in the vicinity of atomic nuclei and, to a much lesser extent, orbital electrons. Any energy carried by the transformed photon in excess of the rest mass energy of the pair is transferred to the particle pair in the form of kinetic energy. The pairs quickly slow to thermal energies and the positron invariably combines with an electron under the influence of attractive Coulombic forces. Upon combination the electron and position annihilate– resulting in two annihilation photons. Annihilation photons equally share the energy equivalent of the positron-electron rest mass and any remaining kinetic energy held by the positron before annihilation. The directions of the emerging photons are such that momentum is conserved. Because annihilation typically occurs at low kinetic energies, photons of energy very close to 0.511 MeV traveling in nearly-exact opposite directions are created. The distance traveled by the positron and electrons is typically on the order of a few millimeters. The time span of the positron slowing down and annihilating is also small– resulting in the annihilation photons emerging nearly coincident in space and time with the pair production interaction[3].

1.3.4 Photon Range

The interaction processes described in Sections 1.3.1-1.3.3 limit the distance a photon will travel in matter. Depending on the energy of the photon and the

charge density of the attenuating medium, photon range can vary roughly from centimeters to meters. The probability (p) that a photon will go without interaction after traveling a given distance (x) in a specific material is governed by Equation 4.

$$p(x) = \exp(-\sigma_t x) \tag{4}$$

where σ_t is the total probability per unit path-length that interaction will occur. It follows that the probability $P(x)$ a photon will travel distance x and then undergo an interaction in a differential distance between x and $x+dx$ is given by Equation 5

$$P(x) = p(x)\sigma_t dx \tag{5}$$

Taking the first spatial moment of Equation 5 we can determine the average distance a photon will travel before interacting– this distance is known as the mean free path (MFP):

$$MFP = \int_{x=0}^{\infty} xp(x)\sigma_t dx = \frac{1}{\sigma_t}. \tag{6}$$

The mean free path can be a useful metric when considering how radiation is likely to behave in a system. If the system is large relative to the MFP, there will be strong interaction and if it is small relative to the MFP there will be little interaction. The correlation between MFP and system dimension also gives rise to the concept of "optical thickness." Optical thickness is defined as distance measured in mean free paths.

Figure 1 displays photon range as a function of energy for several materials common to radiation shielding and detection.

1.4 Interaction of Beta Radiation with Matter

Energetic positrons and electrons lose their energy at a much higher rate than photons. This is due to two processes that depend on the mass of beta particles

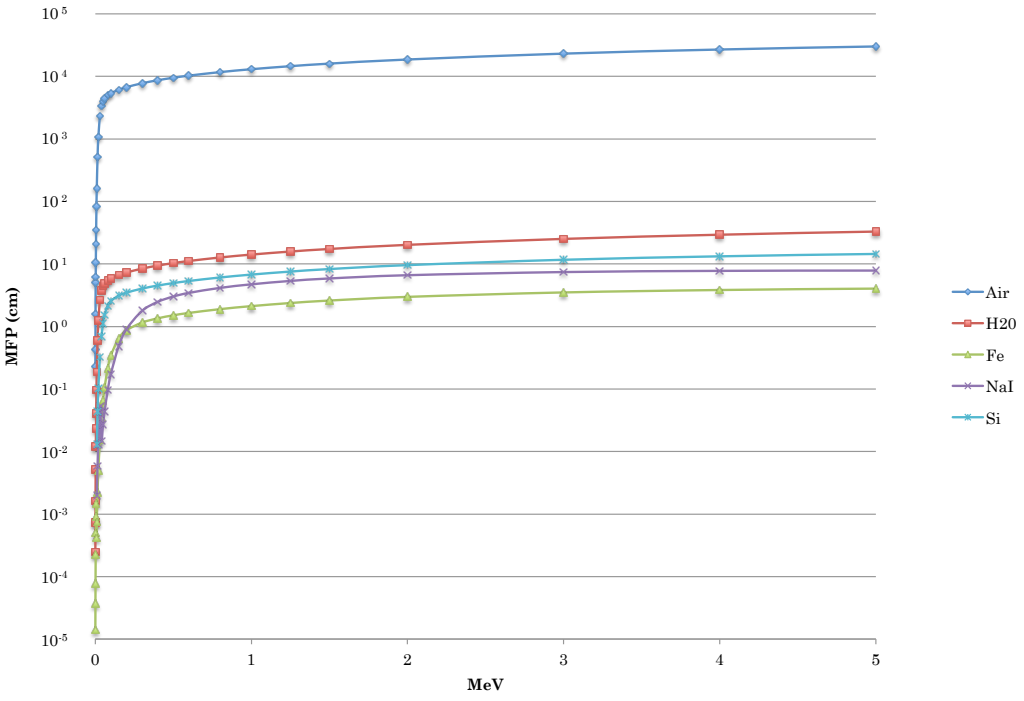

Figure 1: Mean free path of photons in multiple materials [2, Appendix C].

[10, p. 193]. First, because their mass is equal to that of the atomic electrons with which they interact, large energy losses due to collision are kinematically favorable. Secondly, because the mass of beta particles is small compared to the mass of the charged nuclei, abrupt coulombic deflection is possible that results in significant radiative energy loss (bremsstrahlung). Because of these interactions, beta particles follow short, highly-erratic paths as they slow.

1.4.1 Beta Particle Range

The distance traveled by mono-energetic electrons through a material varies from particle to particle due to randomness in the collisions. However, there is a distance beyond which it is assumed no particles will travel. This distance is known as the particle's "range." Range can be measured experimentally or calculated. The latter requires an analysis of the beta particles interactions that accounts for the effects of relativity, quantum mechanics, and classical physics to determine a quantity known as "stopping power". Stopping power describes the amount of energy that is lost per unit length along the track of a beta particle and is a function of the medium of interaction and the energy of the particle. Details on the calculation of stopping power values are discussed thoroughly in reference [10]. Given an equation for stopping power, range can then be calculated using Equation 7

$$R = \int_0^{E_0} \frac{1}{S_{tot}(E)} dE \tag{7}$$

where

$E_0 \equiv$ Incident energy of beta particle

$S_{tot} \equiv$ Total stopping power

Range as a function of incident energy for air and carbon is shown in Figure 2 below.

1.5 Pulse Height Distributions

As a photon undergoes the interactions described in Sections 1.3.1-1.3.3 its energy is transferred to the medium and secondary particles. Examination of the distribution of energy deposited over many photon histories can lead to useful

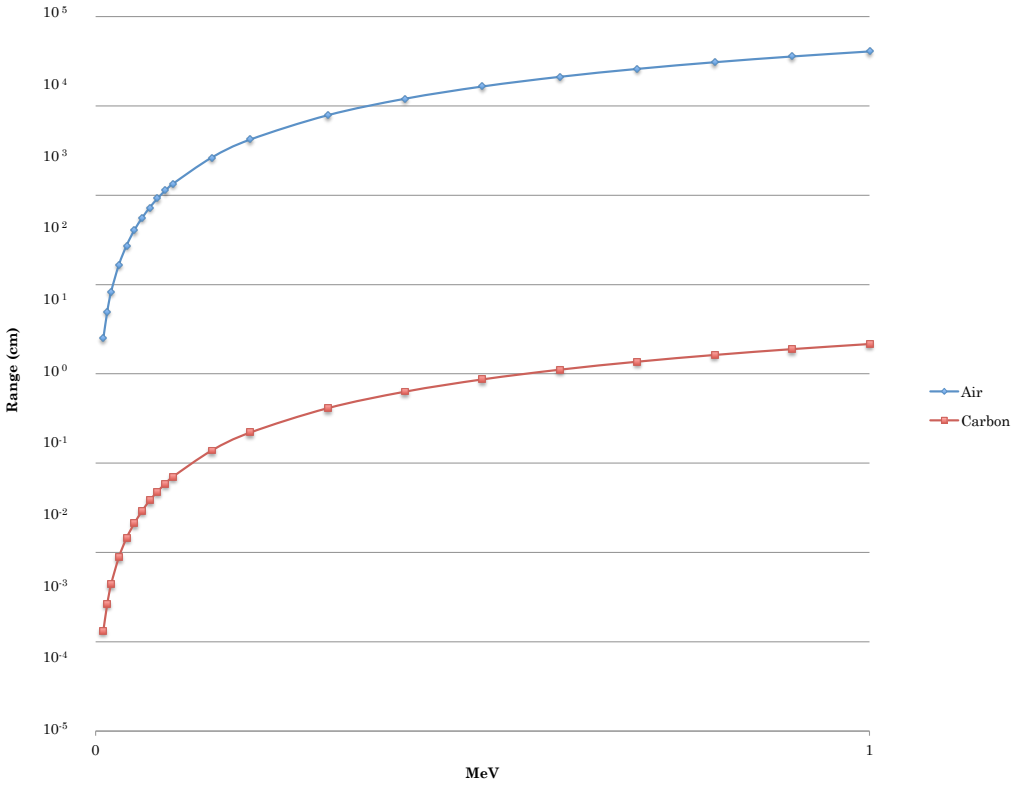

Figure 2: Range of beta particles in air and carbon calculated with Equation 7 [10, p. 738].

information about the origin of the photon and the nature of its interaction.

A common approach to this examination is mapping the distribution of events which deposit a quantity of energy (E). The differential count of events depositing energy E about dE can be interpreted as the rate of change in the total interaction rate ($\frac{dN}{dE}$) or as the rate of interactions depositing energy in dE about E. This distribution is a function of the source particle's energy and the the composition and geometry of the system. In practice the distribution is a piecewise construction where dE is replaced by a range ΔE about E and dN by ΔN. To create a continuous distribution from a measured stepwise distribution, each ΔN is divided

by its respective bin width ΔE. In this thesis distributions will be left in the histogram (not divided by ΔE) format to more clearly demonstrate bin boundaries.

Each of the previously described photon interaction mechanisms (Sections 1.3.1-1.3.3) results in a unique energy deposition signature. The complete distribution of energy deposition is therefore a combination of the signatures from all probable interactions. The following is a description of the resulting features found in PHDs. Each feature can be found labeled in Figure 3.

A) Contribution to the full energy peak (or photo peak) occurs when an incident photon is completely absorbed in the system. This can happen through any interaction mechanism on the condition that the secondary particles (e.g. photo-electrons, Compton scattered photons and electrons, and annihilation photons) are completely absorbed in the system. As system dimensions grow the probability of secondaries being completely absorbed also grows resulting in increased prominence of this peak.

B) Peak B is the X-ray escape peak and is created by the escape of characteristic X-rays following photo-electric absorption of a photon. Characteristic X-rays have a low energy that corresponds to the binding energy of the atom's electron orbitals– usually the K-shell [3, p. 15]. Due to the characteristic X-ray's low energy, it has a range on the order of millimeters in most materials [3, p. 309] and therefore only results in a significant peak in systems with small dimensions.

C) Point C marks the Compton edge. Energy deposition beyond this point is not possible in a single Compton scatter event due to the kinematics of the collision (see Equation 2). A scattered photon can however impart a portion of its energy, between zero and the Compton edge, onto an electron before escaping the system. That spectrum of energy deposition results in the Compton continuum which is

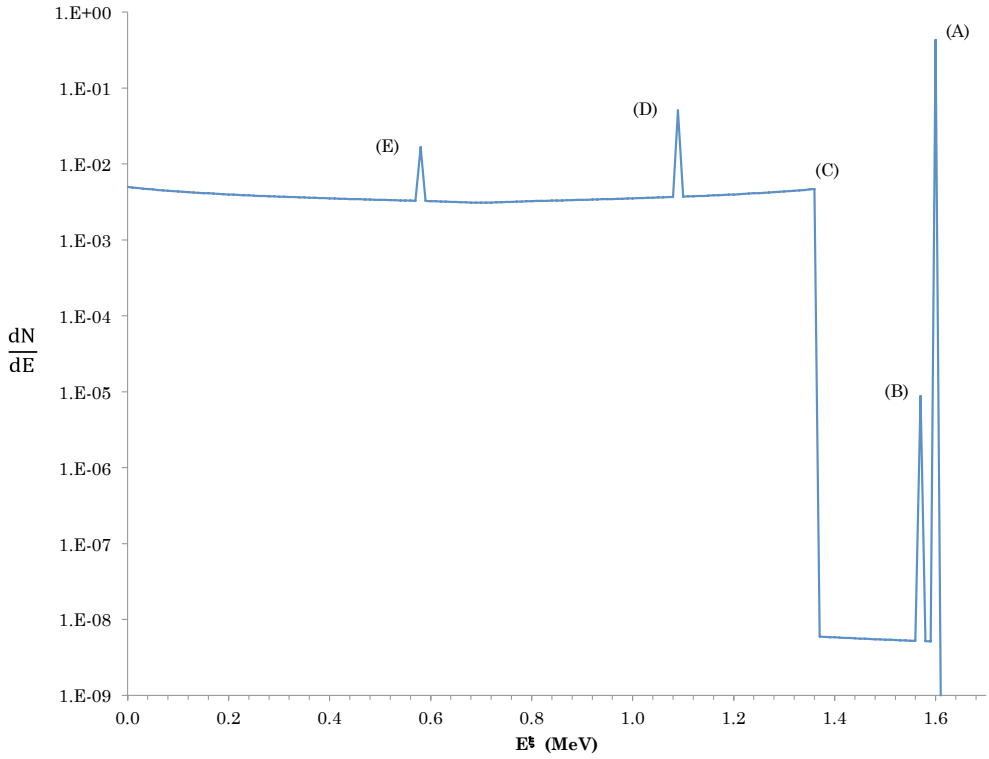

Figure 3: Features of a typical pulse height distribution.

evidenced by the portion of the PHD that spans from point C to the y-axis.

D/E) Peaks D and E are the single and double escape peaks, respectively. They are created by the escape of annihilation photon (Section 1.3.3) and are located 0.511 MeV and 1.022 MeV below the full-energy peak.

1.6 Neutral Particle Transport Equation

The basis of radiation transport is the balance of particles entering and exiting a particular phase space volume in a system. In its most general form, the balance considers particles in an arbitrary phase space volume defined by the particle's

location in the system ($\hat{r}$), direction of travel ($\hat{\Omega}'$), and kinetic energy (E') at time t. The mathematical construction of this balance leads to the neutral particle transport equation. The equation is developed by considering each mechanism which may add particles (sources) or remove particles (sinks) from the phase space volume. Reference [6] provides a thorough derivation. The result of this derivation is the transport equation:

$$\begin{aligned} &\frac{dN}{dt}(E,\hat{\Omega},\hat{r},t) + \hat{\Omega}\cdot\nabla\psi(E,\hat{\Omega},\hat{r},t) + \sigma_t(\hat{r},E)\psi(E,\hat{\Omega},\hat{r},t) = \\ &\int_{4\pi}\int_0^\infty \psi(E',\hat{\Omega}',\hat{r},t)\sigma_s(E'\to E,\hat{\Omega}'\to\hat{\Omega})dE'd\hat{\Omega}' + \hat{S}(E,\hat{\Omega},\hat{r},t) \end{aligned} \tag{8}$$

The first term of the left hand side (LHS) is the time rate of change of particles at $(E,\hat{\Omega},\hat{r},t)$. This quantity is sometimes written as the equivalent expression $\frac{1}{v}\frac{d\psi(E,\hat{\Omega},\hat{r},t)}{dt}$. The next term on the LHS is the divergence of the angular flux. This term accounts for particles streaming uncollided out of the phase space volume about position $\hat{r}$ and direction $\hat{\Omega}$. The following may be useful to understand the physical meaning of this term. Before simplification, this term is given as

$$\int_S \psi(E,\hat{\Omega},\hat{r},t)\hat{\Omega}\cdot d\hat{n} \tag{9}$$

where $\hat{n}$ is a unit vector normal to the surface of the differential volume. It is more clearly seen that the dot product of the angular current density and the surface normal vector account for particles streaming out of dV. This quantity is transformed into the form seen in (4) by the application of Gauss' Theorem which states

$$\int_S \hat{A}(\hat{r})\cdot d\hat{n} = \int_V \nabla\cdot\hat{A}(\hat{r})dV \tag{10}$$

In our case

$$\hat{A}(\hat{r}) = \psi(E, \hat{\Omega}, \hat{r}, t)\hat{\Omega}$$

and (11)

$$\nabla \cdot \psi(E, \hat{\Omega}, \hat{r}, t)\hat{\Omega} = \hat{\Omega} \cdot \nabla\psi(E, \hat{\Omega}, \hat{r}, t)$$

The final term on the LHS is the total rate of interactions of any type occurring in the phase space volume $(E, \hat{\Omega}, \hat{r}, t)$. This term is a sink because an interaction of any kind will remove particles from $(E, \hat{\Omega}, \hat{r}, t)$. On the right hand side are the source terms. These include the total number of particles scattering into $(E, \hat{\Omega}, \hat{r}, t)$ from all other energies (E') and directions $(\hat{\Omega}')$ at location $\hat{r}$, and any particles coming from external sources or multiplication, $\hat{S}$. In other words, particles arrive at $(E, \hat{\Omega}, \hat{r}, t)$ from scattering events or an external source and leave $(E, \hat{\Omega}, \hat{r}, t)$ by streaming away or undergoing any type of collision. Any difference between the sinks and the sources results in a change in the number of particles in the phase space volume, $(\frac{dN}{dt})$.

1.6.1 Slab Geometry Transport Equation

The slab-geometry transport equation can be derived by integrating the transport equation over the azimuthal angle; the polar angle θ is relative to the single dimension along which there is spatial variation. With ψ no longer a function of the azimuthal angle ϕ, the streaming term is reduced as seen in Equation 12. Here we introduce $\mu = \cos(\theta)$.

$$\hat{\Omega} \cdot \nabla\psi(E, \hat{\Omega}, \hat{r}, t) = \mu\frac{d\psi(E, \mu, x)}{dx} \tag{12}$$

Similarly, the RHS reduces to Equation 13.

$$\int_{\phi=0}^{2}\int_{\theta=0}^{\pi}\int_{0}^{\infty}\psi(E',\hat{\Omega}',\hat{r})\sigma_s(E'\rightarrow E,\hat{\Omega}'\rightarrow\hat{\Omega})dE'd\theta d\phi+\hat{S}(E,\theta,x)= \\ \int_{\theta=-0}^{\pi}\int_{0}^{\infty}\psi(E',\theta',x)\sigma_s(E'\rightarrow E,\theta'\rightarrow\theta)dE'd\theta'+\hat{S}(E,\theta,x) \tag{13}$$

Substituting μ again, the final result is given by Equation 14

$$\mu\frac{d\psi(E,\mu,x)}{dx}+\sigma_t\psi(E,\mu,x)= \\ \int_{\mu=-1}^{1}\int_{0}^{\infty}\psi(E',\mu',x)\sigma_s(E'\rightarrow E,\mu'\rightarrow\mu)dE'd\mu'+\hat{S}(E,\mu,x) \tag{14}$$

Equation 14 is the slab-geometry transport equation. The transport equation in this form will be used for the remainder of this thesis.

1.7 Deterministic Transport

Deterministic solutions to the transport equation are found by solving a linear system of equations for a discrete set of flux values. The form of this linear system of equations is dependent on the method of discretization employed in each of the independent variables. Equation 15 is the discretized version of the steady-state, slab-geometry transport equation obtained by integrating the transport equation over a spatial cell.

$$\mu_n\int_{x_{i-1/2}}^{x_{i+1/2}}\left.\frac{d\psi}{dx}\right|_{g,n}dx+\Delta x_i\sigma_{t,g,i}\psi_{g,n,i}= \\ \Delta x_i\sum_{n'=1}^{N}\sum_{g'=1}^{G}\sigma_s(g'\rightarrow g,n'\rightarrow n)\psi_{g',n',i}+\Delta x_i S_{g,n,i} \tag{15}$$

where

$\mu_n \equiv$ direction cosine of the n^{th} angular ordinate

$g \equiv$ energy group index

$i \equiv$ the i^{th} spatial cell

$N \equiv$ number of angular ordinates

$G \equiv$ number of energy groups

$S \equiv$ any external source

Discretization of the transport equation variables is discussed in the following sections.

1.7.1 Energy Discretization

Discretization of energy dependent quantities (i.e. cross sections, flux, yield, etc.) is usually performed using the multigroup method, where the group boundaries are to encompass domains on which there is limited change in the dependent variables. Groups are indexed using the subscript g, with the highest energy group associated with the first index (group 1) and the last group given by the subscript G. Group boundaries are denoted with half-integer values, such as $E_{g\pm\frac{1}{2}}$.

Group-averaged cross sections are created by averaging the energy-dependent cross sections over the chosen energy bounds. If energy dependent flux information is available, it is used to flux-weight the cross-sections, which produces accurate data over a wider energy range. If the flux profile is unknown, it is assumed constant and bins should be chosen to limit the changes in the magnitude of the flux over the range. The energy averaged cross-section $\sigma_{X,g}$ for any reaction (X) is given by Equation 16.

$$\sigma_{X,g} = \frac{\int_{E_{g+\frac{1}{2}}}^{E_{g-\frac{1}{2}}} \sigma_X(E)\phi(E)dE}{\int_{E_{g+\frac{1}{2}}}^{E_{g-\frac{1}{2}}} \phi(E)dE} \tag{16}$$

$$\psi_g = \int_{E_{g+\frac{1}{2}}}^{E_{g-\frac{1}{2}}} \psi(E)dE \tag{17}$$

1.7.2 Functional Expansion of Discrete Cross Sections

In numerical transport simulation, the dependence of the scattering cross section on the scattering angle cosine ($\mu_0 = \hat{\Omega} \cdot \hat{\Omega}$) is commonly expanded into a set of Legendre polynomials– seen here as derived by Bell [4, p. 175]. Exact equality of the cross section and its expansion occurs when the series seen in the RHS of Equation 18 is summed over its infinite terms. In practice, this series is truncated to $L + 1$ terms.

$$\begin{aligned}\sigma_s(E' \to E, \mu' \to \mu) &= \sigma_s(E' \to E, \hat{\Omega}' \cdot \hat{\Omega}) = \sigma_s(E' \to E, \mu_0) \\ &= \sum_{l=0}^{\infty} \frac{2l+1}{4\pi} \sigma_{s,l}(E' \to E) P_l(\mu_0)\end{aligned} \tag{18}$$

In Equation 18 P_l is a Legendre polynomial whose form depends only on the particular l and is crafted such that the summation is exactly equal to the function when they are evaluated at a particular value– in our case of angle.

$$P_0(\mu) = 1$$
$$P_n(\mu) = \frac{1}{2^n n!}\frac{d^n}{d\mu^n}(\mu^2 - 1)^n \tag{19}$$

for $n = 1, 2, ...$

The expansion coefficient σ_l is given by Equation 20.

$$\sigma_l(E' \to E) = 2\pi \int_{-1}^{1} \sigma_s(E' \to E, \mu_0) P_l(\mu_0) d\mu_0 \tag{20}$$

Using the Legendre expansion, the discrete one-dimensional transport equation can be written as:

$$\mu_n \int_{x_{i-1/2}}^{x_{i+1/2}} \left.\frac{d\psi}{dx}\right|_{g,n} dx + \Delta x_i \sigma_{t,g,i} \psi_{g,n,i} =$$
$$\Delta x_i \sum_{l=1}^{L} \frac{(2l+1)}{2} \sum_{g'=1}^{G} \sigma_{s,l,g' \to g,i} \phi_{l,g',i} P_l(\mu_n) + \Delta x_i S_{g,n,i} \tag{21}$$

where

$$\phi_{l,g',i} = \sum_{n'=1}^{N'} \psi_{g',n',i} P_l(\mu_{n'}) w_{n'} \tag{22}$$

$$\psi_{g',n',i} = \frac{1}{\Delta x_i} \int_{E_{g'+\frac{1}{2}}}^{E_{g'-\frac{1}{2}}} \int_{x_{i-\frac{1}{2}}}^{x_{i+\frac{1}{2}}} \psi(E, \mu_{n'}, x) dE dx \tag{23}$$

1.7.3 Linear Characteristic Method in 1-D

The linear characteristic method (LC) is a deterministic method which approx-

imates the source distribution in each cell as a linear function of the spatial variable (x). Using the linear source distribution and incident angular flux, Equation 24 gives the angular flux distribution across a cell. Equation 25 defines the source distribution.

Adams [7] outlines the LC process which includes the following steps:

1. Construct $\psi_n(x)$ on incoming surfaces of the cells
2. Construct $S_{n,i}(x)$ using the latest source moment ($s_{n,i}$ and $s^x_{n,i}$)
3. Compute $\psi_{n,x_{i+\frac{1}{2}}}$ using the analytic $\psi_n(x)$ obtained from Equation 24
4. Solve the cell balance and first spatial moment equations (Equations 29 and 30) for the angular flux moments $\psi_{n,i}$ and $\psi^x_{n,i}$
5. Use the new angular flux moments to create new source moments $q_{n,i}$ $q^x_{n,i}$.

The first step yields an expression for the outgoing edge angular flux in terms of the incoming angular flux and cell sources:

$$\psi_n(x_{i-\frac{1}{2}} + \Delta x_i) = \psi_{n,i-\frac{1}{2}} \exp(-\sigma_t \frac{\Delta x_i}{|\mu_n|}) + \int_0^{\Delta x_i} S_{n,i}(x) \exp(-\sigma_t x) dx, \tag{24}$$

where

$$S_{n,i}(x) = s_{n,i} + s^x_{n,i} \frac{2(x - x_i)}{\Delta x_i} \tag{25}$$

The source moments created in Equations 26-27 contain external and internal (scattering) source moments– as shown based on isotropic scattering:

$$s_{n,i} = q_{ext,n,i} + \frac{\sigma_{s,0,i}}{2} \sum_{n'=1}^{N} \psi_{n',i} w_{n'} \tag{26}$$

$$s^x_{n,i} = q^x_{ext,n,i} + \frac{\sigma_{s,0,i}}{2} \sum_{n'=1}^{N} \psi^x_{n',i} w_{n'} \tag{27}$$

$$q_{ext,n,i} = \frac{1}{\Delta x_i} \int_{x_{i-\frac{1}{2}}}^{x_{i+\frac{1}{2}}} q_{ext,n}(x) dx \tag{28}$$

$$\frac{\mu_n}{\Delta x_i} [\psi_{n,x_{i+\frac{1}{2}}} - \psi_{n,x_{i-\frac{1}{2}}}] + \sigma_{t,i} \psi_{n,i} = q_{n,i} \tag{29}$$

$$\frac{3\mu_n}{\Delta x_i} [\psi_{n,x_{i+\frac{1}{2}}} + \psi_{n,x_{i-\frac{1}{2}}} - 2\psi_{n,i}] + \sigma_{t,i} \psi^x_{n,i} = q^x_{n,i} \tag{30}$$

1.8 Deterministic Pulse Height Distribution Simulations

Using deterministic solutions of the multigroup, slab geometry S_N equations, Benz and Palmer were able to simulate a PHD [1]. To explain their approach, we first consider a system with mono-energetic source particles at energy E_S. In such a system, any portion of the flux leaving the system at energy E deposits an energy E^ξ equal to $E_S - E$. With the number of particles leaving the problem with energy E given by the outgoing partial current $j^+(E)$, we can write Equation 31 for the differential pulse height distribution for all energy deposition below E_S:

$$\left.\frac{dN}{dE}\right|_{(E_S - E)} = j^+(E), \qquad 0 < E \leq E_S. \tag{31}$$

From this equation, it is apparent that it is not valid where $E = E_S$ because $j^+(0)$ has no meaning. Full energy deposition events are the result of absorption of source particles and their contribution is given by Equation 32 which is the reaction rate for absorption.

$$\left.\frac{dN}{dE}\right|_{E_S} = \int_{x=0}^{L}\int_{E=0}^{E_S} \sigma_a(E,x)\phi(E,x)dEdx$$

$$= j^-(E_S) - \int_{E=0}^{E_S} j^+(E)dE \tag{32}$$

Using Equations 31 and 32 it is possible to construct a complete PHD given a mono-energetic source. If the source is not mono-energetic, the situation becomes more complex because the escaping current and absorption can correspond to particles of any energy in the source-energy range. The following section explains how Benz and Palmer account for this possibility.

1.8.1 $\frac{dN}{dE}$ with Multiple Source Energies

To correlate absorbed and escaped particles with their respective starting energies, Benz kept separate scattered elements of the flux and tracked components of the flux from source to sink.

A converged solution (Ψ) of the transport equation is the linear combination of flux components ψ^s that have undergone some number of collisions s.

$$\Psi = \psi^0 + \psi^1 + \psi^2 + ... = \sum_{s=0}^{\infty} \psi^s \tag{33}$$

To illustrate, consider the time-independent slab-geometry transport equation (independent variables excluded for clarity):

$$\mu\frac{\partial\Psi}{\partial x}+\sigma_t\Psi=$$
$$\int_{\mu'=-1}^{1}\int_{E'=0}^{\infty}\sigma_s(E'\to E,\mu'\to\mu)\Psi(E',\mu',x)dE'd\mu'+S(E,\mu,x) \tag{34}$$

If we define a source q^s which changes as a function of the number of collisions experienced by the radiation:

$$q^s=\begin{cases} S(E,\mu,x), & s=0,\\ \int_{\mu'=-1}^{1}\int_{E'=0}^{\infty}\sigma_s(E'\to E,\mu'\to\mu)\psi^{s-1}(E',\mu',x)dE'd\mu', & s>0. \end{cases} \tag{35}$$

then we can decompose Equation 36 into a system of equations for the collided components of ψ:

$$\begin{aligned} \mu\frac{\partial\psi^0}{\partial x}+\sigma_t\psi^0&=q^0\\ \mu\frac{\partial\psi^1}{\partial x}+\sigma_t\psi^1&=q^1\\ &\vdots\\ \mu\frac{\partial\psi^s}{\partial x}+\sigma_t\psi^s&=q^s \end{aligned} \tag{36}$$

Benz maintained the correlation between particles escaping the system at energy E and their respective source energies E_S by calculating the fraction of particles at each value of $\psi^s(E)$ which scattered to that state from a starting energy E'– doing so for each E' from $E'=E_S$ through the iteration in which a particle was absorbed or escaped. The product of those fractional scattering contributions and the outgoing current or absorption during each respective iteration then determined the number of particles leaving the system at energy E which started at energy E_S.

Benz accomplishes this using two matrices. The first is the "scattered source matrix",

$$\tilde{\sigma}_{s,m,g}\phi_m^{(s)} = \frac{\sigma_{s,m,g}\phi_m^{(s)}}{\sum_{g'=1}^{g} \sigma_{s,g'\to g}\phi_{g'}^{(s)}}, \tag{37}$$

which calculates the fractional contribution of a scattering event from group m to group g to the total scattering source in group g. The second matrix uses data in the scattered source matrix to generate the respective fractions of particles starting in source group l, undergoing s collisions, and arriving in group g. The matrix defined by

$$f_{l,g}^{(s)} = \sum_{m=l}^{g} \left[f_{l,g}^{(s-1)} \left(\tilde{\sigma}_{s,l,m}\phi_l^{((s-1)} \right) \right], \tag{38}$$

with

$$f_{l,g}^{(0)} = \begin{cases} 1, & \phi_l^{(0)} \neq 0 \text{ and } l = g, \\ 0, & \text{otherwise.} \end{cases} \tag{39}$$

1.8.2 Energy Bin Mapping for $\frac{\Delta N}{\Delta E}$ Histograms

To map the energy deposited by the flux as through scatter and absorption Benz constructed deposition energy bins based on the initial and terminal energy groups of the flux components. Energy group g' has a width defined as $\Delta E_{g'} = E_{g',high} - E_{g',low}$, where $E_{g',high}$ and $E_{g',low}$ represent the high and low energy boundaries of the initial bin. In a downscatter event from group g' to g the corresponding range of the energy loss was given by:

$$\Delta E_{g',g} = \Delta E_{g',g,high} - \Delta E_{g',g,low}$$

$$= (E_{g',high} - E_{g,low}) - (E_{g',low} - E_{g,high}). \quad (40)$$

[**Note:** Energy deposited is shown here in the original author's notation $\Delta E_{g',g}$. Elsewhere in this thesis the E^{ξ} superscript has been adopted to differente between flux energy and deposition energy.] By repeatedly employing Equation 40 for all values of g' and g, all possible energy losses from scattering routes were determined.

1.8.3 The Pair Production Problem

The process developed by Benz to simulate PHDs was demonstrated to work well for systems where particle collisions do not result in prompt multiplication. However, if such multiplication does exist, complications arise in maintaining a tally of energy deposited by flux components. In the multiplying process, energy is carried away by progeny of the reaction– energy which can no longer be associated with the incident flux. Pair production is a prime example of this phenomenon. Incident radiation with energy in excess of 1.022 MeV may create a positron-electron pair. The pair will quickly deposit its kinetic energy and a pair of annihilation photons will be born. In Benz's scheme, the process appears to be one in which the incident photon has downscattered to the energy group bounding 0.511 MeV as two photons. There is no way to then sum the energy deposited by the pair of annihilation photons with that deposited by the incident photon. The result is the introduction of an artificial source of independent annihilation photons. Figure 4 is a histogram for the PHD associated with treatment of annihilation photons as downscatter. No single or double escape peaks are visible because there is no correlation between the incident particle and the annihilation photons. The prominent

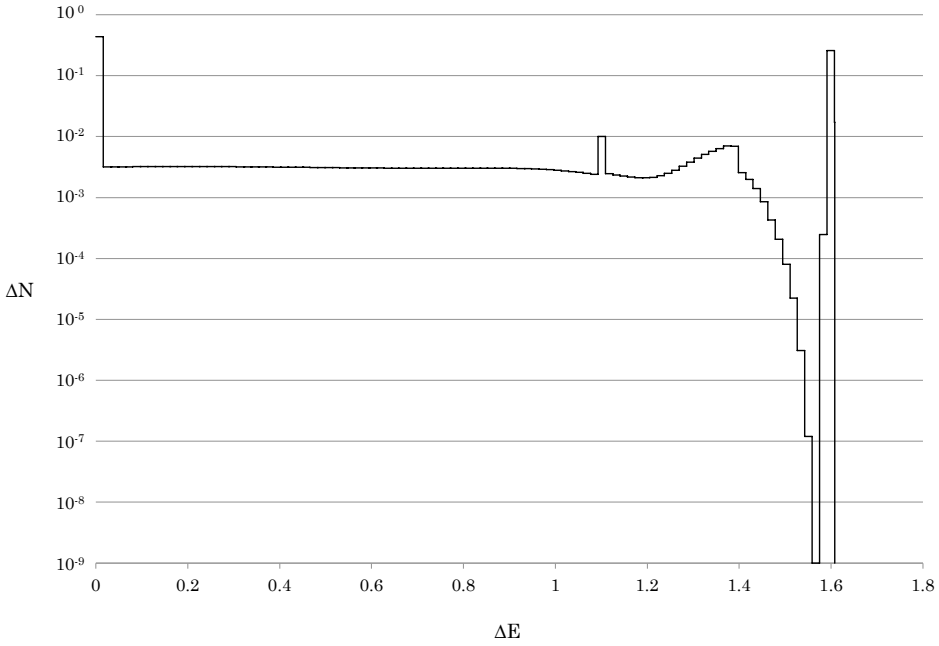

Figure 4: Histogram for a deterministically generated PHD with annihilation photons treated as downscatter. A 1.6 MeV source is incident on the left side of a 5cm thick NaI slab. Data generated using S_{32} angular quadrature, 5 cells, and 100 energy groups with a 0.001MeV cutoff.

peak on $[1.081, 1.097]$ is created by the escape of "scattered" 0.511 MeV photons. The peak is located where a single escape peak is expected cannot be interpreted as such.

1.9 Thesis Overview

The remainder of this thesis is organized into the following sections:

II. **Methods** - In this section we will discuss two candidate treatments for pair production in deterministic pulse height distribution simulations. We also

introduce an alternative interpretation of energy deposition distributions resulting from within-group scatter and downscatter events.

III. **Results** - In this section we present data generated using the pair production treatments and energy deposition distributions presented in the Methods section. Distributions are presented graphically and areas under the double, single, and zero escape peaks are presented tabularly. Results of an iteration parameter study are also given. This parameter study was conducted to determine the number of iterations on the scattering source required for convergence of the test problems.

IV. **Conclusions** - Here, we discuss all of the data presented in the Results section, including: a comparison of the energy deposition distributions proposed in the Methods section with those used in previous works, an evaluation of the two candidate pair production treatments, and the implications of the iteration parameter study. We close with general conclusions and suggestions for future work.

2 Methods

2.1 Introduction

The treatment of pair production presented in this thesis is based on the separation of transport solutions for the incident flux and its scattered components from the transport of the annihilation pairs created by incident flux. The quantities related to the transport of the incident flux and scattered components will be designated "primary." Quantities related to individual annihilation photons will be designated "511" and those related to annihilation photon pairs will be designated by "511-pair." In this section E with or without subscript is the photon energy and E^{ξ} with or without subscript refers to energy deposited in the background medium.

Figure 5 shows the flow of the process used to create a PHD that accounts for pair production effects.

2.2 Opposing-Ordinate PHD Combination Method

The first step in opposing-ordinate PHD combination is producing a PHD for the primary flux. This is accomplished as discussed in Section 1.8 with one change. Here, the transport solutions for all scattering iterations will be calculated excluding the annihilation photon source. This is done by modifying the source term used in the RHS of the balance equation. Equation 41 shows the balance equation with a source that includes both scatter and the production of annihilation photons.

$$\mu_n(\psi_{g,n,i-\frac{1}{2}} - \psi_{g,n,i+\frac{1}{2}}) + \sigma_{t,g,i}\psi_{g,n,i}\Delta x_i = \sum_{g'=1}^{g}\sum_{n'=1}^{N}\psi_{g',n',i}\Sigma_{g'\to g,n'\to n,i}\Delta x_i \qquad (41)$$

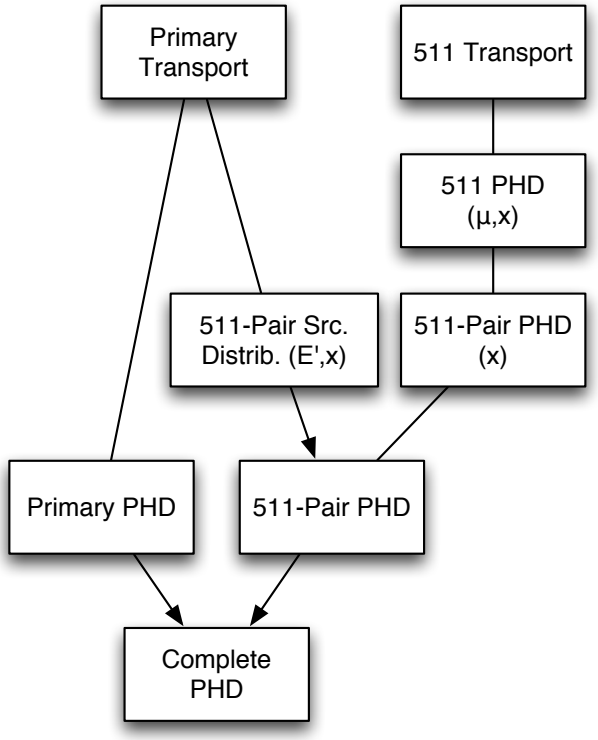

Figure 5: Opposing ordinate combination treatment for pair production.

In this equation, $\Sigma_{g' \to g,n' \to n,i}$ is a transfer cross section given by Equation 42.

$$\Sigma_{g' \to g,n' \to n,i} = \sigma_{s,g' \to g,n' \to n,i} + 2 * \sigma_{pp,g' \to g,n' \to n,i} \tag{42}$$

where

$\sigma_{s,g' \to g,n' \to n,i} \equiv$ scatter cross section

$\sigma_{pp,g' \to g,n' \to n,i} \equiv$ pair production cross section

The modified source term used in the primary PHD simulation is shown in the RHS of Equation 43 where $\Sigma_{g' \to g,n' \to n,i}$ is replaced by $\sigma_{s,g' \to g,n' \to n,i}$. In the LHS of

both equations the pair production cross section is included in σ_t.

$$\mu_n(\psi_{g,n,i-\frac{1}{2}} - \psi_{g,n,i+\frac{1}{2}}) + \sigma_{t,g,i}\psi_{g,n,i}\Delta x_i = \sum_{g'=1}^{g}\sum_{n'=1}^{N}\psi_{g',n',i}\sigma_{s,g'\to g,n'\to n,i}\Delta x_i \quad (43)$$

where

$$\sigma_{t,g,i} = \sigma_{s,g,n'\to n,i} + \sigma_{a,g,i} + \sigma_{pp,g,i}$$

Given a unit source specification and the use of the modified source term, a histogram based on a converged transport solutions should sum to $1 - S_{PP}$ where S_{PP} is the probability of pair production in the system.

Next, a PHD is generated for the energy deposition of annihilation pairs in the system. This starts with PHDs that are generated based on unit sources at each ordinate, in each cell. Each PHD is generated independently (resulting in $N \times I$ distributions where N and I are the angular quadrature order and total number of cells respectively). The PHDs of diametrically-opposing ordinates in each cell are then summed to form new distributions (with a resulting range of [0,1.022MeV]), because opposing PHDs represent PHDs for the constituent photons of annihilation pairs whose energy deposition must be treated collectively.

The combined distributions are then integrated over angle. The result is a set of PHDs which give the collective energy deposition response for uniformly generated annihilation pairs in each cell. The details of this construction are discussed is Sections 2.2.1 and 2.3. The PHDs for annihilation pairs in each cell are then weighted by the pair production source term S_{pp} in that cell and combined– giving an effective PHD for pair production in the system. Lastly, the 511-pair PHD and primary PHD are combined to created a PHD which accounts for the effects of pair production.

2.2.1 Opposing PHD Combination

In opposing-ordinate PHD combination, converged transport solutions are used to create a set of PHDs which each reflect the energy deposition behavior of a source originating at a particular angle and cell. The PHD corresponding to each source is then combined with the PHD of the source originating in the same cell and opposite direction. The combination of 511 PHDs is based on the following reasoning: if one photon of an annihilation pair traveling in direction μ deposits energy $E^{\xi(1)}$ and the other traveling in direction $-\mu$ deposits energy $E^{\xi(2)}$, the collective energy deposition is $E^{\xi'}$. The probability that energy $E^{\xi'}$ will be deposited is given by the collective probability of $E^{\xi(1)}$ and $E^{\xi(2)}$ taking values such that $E^{\xi(1)} + E^{\xi(2)} = E^{\xi'}$. Let P^1, P^2, and P^3 be pulse height distributions ($\frac{dN}{dE}$) for individual annihilation photon sources in directions μ, $-\mu$, and the combined PHD for that direction set, respectively. The probability that the pair will deposit energy $E^{\xi'}$ is given by Equation 44.

$$P^3(E^{\xi'}) = \int_{E^{\xi}=0}^{E^{\xi'}} P^1(E^{\xi(1)}) P^2(E^{\xi(2)}) dE^{\xi(1)} \tag{44}$$

where $E^{\xi(2)} = E^{\xi'} - E^{\xi(1)}$.

In a system with discrete energy groups, Equation 44 is expressed as a normalized summation as shown in Equation 46. Equation 45 sums the products of discrete probabilities that correspond to a unique resultant energy bin defined by Equation 47. This approach is dependent on the use of an equivalent, uniform energy group structure for distributions P^1 and P^2.

$$\acute{P}^3_{h'} = \sum_{h=1}^{h'} P^1_h P^2_{h'-h+1} \tag{45}$$

$$P^3_{h'} = \frac{\acute{P}^3_{h'}}{\sum_{h'=1}^{H'} \acute{P}^3_{h'}} \tag{46}$$

$$\begin{aligned} E^{\xi}_{h'+\frac{1}{2}} &= E^{\xi}_{h+\frac{1}{2}} + E^{\xi}_{(h'-h+1)+\frac{1}{2}} \\ E^{\xi}_{h'-\frac{1}{2}} &= E^{\xi}_{h-\frac{1}{2}} + E^{\xi}_{(h'-h+1)-\frac{1}{2}} \end{aligned} \tag{47}$$

where

$$h \equiv \text{the index of the discretized } E^{\xi}$$
$$h' \equiv \text{the index of the discretized } E^{\xi'}$$

The bin width of h' is given by Equation 47 and is the sum of bin widths ΔE^{ξ}_{h} and $\Delta E^{\xi}_{(h'-h+1)}$ from the respective group structure of the individual annihilation photon PHDs (P^1 and P^2). This broadening can have a significant impact on the resolution of the resulting distribution. Care should be taken when choosing bin structures of P^1 and P^2 to ensure adequate resolution in P^3.

2.2.2 Angular Combination of 511-Pair PHDs

After combining the distributions of opposing ordinates to create the P^3 distributions discussed in the previous section, the PHDs are combined in each cell to produce an effective PHD for annihilation pairs generated at that location. Let $\bar{P}(E^{\xi'}, x)$ be that distribution integrated over half the angular domain used in transport because opposing angles have been combined.

$$\bar{P}(E^{\xi'}, x) = \int_{\mu=0}^{1} P^3(E^{\xi'}, \mu, x) d\mu \tag{48}$$

Discretized values of $\bar{P}(E^{\xi'}, x)$ are given by the summing the products of $P^3_{h',n,i}$ and appropriate quadrature weights– where each $P^3_{h',n,i}$ is given by Equation 46.

$$\bar{P}_{h',i} = \sum_{n=1}^{\frac{N}{2}} \frac{w(n)}{2} P^3_{h',n,i} \tag{49}$$

Quadrature weight is halved because two ordinates ($n(\mu)$ and $n(-\mu)$) go into each $P^3_{h',n,i}$ value.

Developing effective PHDs for annihilation photons for each cell is computationally costly. However, for a given geometry and material composition the problem only needs to be solved once because the $\bar{P}_{h',i}$ distribution is not dependent on the source.

2.3 Modified First-Flight Approximation

An approximation can be used to estimate the single, double, and zero escape peaks. The approximation does not provide distribution information between these peaks, but is much less computationally intensive than the solution of the transport equation. This approach is based on first flight behavior and is applicable because deposition in the peaks is largely governed by the probabilities of uncollided escape and absorption. Table 1 shows the combinations of possible outcomes for annihilation pair photons. In Table 1, P_{Esc} represents the probability that a photon escapes the problem without collision, P_{Abs} represents the probability that a photon is absorbed in the system, and P_{Scat} represents the probability that a

photon will scatter in the system and escape with some fraction of its starting energy.

First Flight Pair Outcomes		
Outcome	E^{ξ}	Peak
$P^1_{Esc} \cap P^2_{Esc}$	$E'_{g\pm\frac{1}{2}} - 1.022MeV$	(DE)
$P^1_{Esc} \cap P^2_{Abs}$	$E'_{g\pm\frac{1}{2}} - 0.511MeV$	(SE)
$P^1_{Esc} \cap P^2_{Scat}$	Unknown	–
$P^1_{Abs} \cap P^2_{Esc}$	$E'_{g\pm\frac{1}{2}} - 0.511MeV$	(SE)
$P^1_{Abs} \cap P^2_{Abs}$	$E'_{g\pm\frac{1}{2}}$	(ZE)
$P^1_{Abs} \cap P^2_{Scat}$	Unknown	–
$P^1_{Scat} \cap P^2_{Esc}$	Unknown	–
$P^1_{Scat} \cap P^2_{Abs}$	Unknown	–
$P^1_{Scat} \cap P^2_{Scat}$	Unknown	–

Table 1: Annihilation pair outcomes. Superscripts 1 and 2 designate the two photons in an annihilation pair.

First-flight probabilities for the known outcomes of Table 1 are given by Equations 50-52 and d_1 and d_2 in the related Equation 53 are the straight-line distances to the system boundary in directions μ and $-\mu$. The superscript is used to indicated the number of scattering events (0=uncollided, for example). Probabilities without scatter order designation should be taken to be after any number of scattering events.

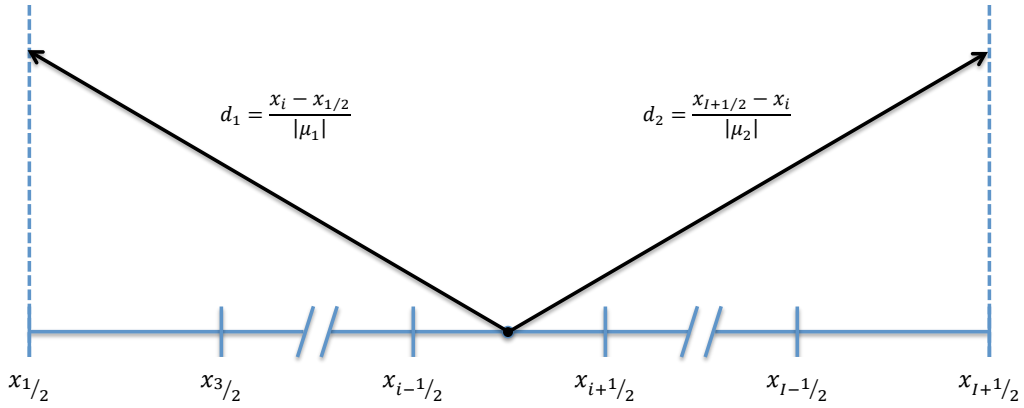

Figure 6: Distances to boundaries for opposing annihilation photon trajectories.

$$P_{DE} = \frac{\int_{x=x_{\frac{1}{2}}}^{x_{I+\frac{1}{2}}} \int_{\mu=-1}^{1} P^1_{Esc} P^2_{Esc} d\mu dx}{\int_{x=x_{\frac{1}{2}}}^{x_{I+\frac{1}{2}}} \int_{\mu=-1}^{1} d\mu dx} \tag{50}$$

$$P_{SE} = \frac{\int_{x=x_{\frac{1}{2}}}^{x_{I+\frac{1}{2}}} \int_{\mu=-1}^{1} P^1_{Esc} P^2_{Abs} + P^1_{Abs} P^2_{Esc} d\mu dx}{\int_{x=x_{\frac{1}{2}}}^{x_{I+\frac{1}{2}}} \int_{\mu=-1}^{1} d\mu dx} \tag{51}$$

$$P_{ZE} = \frac{\int_{x=x_{\frac{1}{2}}}^{x_{I+\frac{1}{2}}} \int_{\mu=-1}^{1} P^1_{Abs} P^2_{Abs} d\mu dx}{\int_{x=x_{\frac{1}{2}}}^{x_{I+\frac{1}{2}}} \int_{\mu=-1}^{1} d\mu dx} \tag{52}$$

where

P_{DE} $\equiv$ The fraction of annihilation source photons that both escape without interaction

P_{SE} $\equiv$ The fraction of annihilation source photons in which one particle escapes without interaction and the other is absorbed

P_{NE} $\equiv$ The fraction of annihilation source photons that are both absorbed

The first flight escape probabilities used in Equations 50 and 51 are given by Equation 53.

$$P_{esc}^{1} = \exp(-\sigma_t d_1)$$
$$P_{esc}^{2} = \exp(-\sigma_t d_2) \tag{53}$$

$$P_{abs}^{1} = (1 - \exp(-\sigma_t d_1))(\frac{\sigma_a}{\sigma_t})$$
$$P_{abs}^{2} = (1 - \exp(-\sigma_t d_2))(\frac{\sigma_a}{\sigma_t}) \tag{54}$$

The absorption probabilities in Equations 51 and 52 are the probabilities of photons being absorbed after undergoing any number of scattering events. However, without converged multi-scatter transport solutions, P_{Abs} cannot be determined exactly in a system where scattering is present. Much work has been done to estimate total escape and absorption (where total denotes summation over all scattered components) probabilities for uniform isotropic source distributions [6, p. 420]. This work was done for neutron transport where spatially uniform isotropic distributions are common. For this analysis we assume that the source is spatially uniform and isotropic for scattered components beyond the first collision. This assumption may be acceptable due to the isotropic nature of annihilation photon production and the generally small optical thickness of detector materials for incident radiation at energy above 1.022 MeV. No assumptions are required for the first flight because the spatial distribution is given by the annihilation pair source distribution defined later in Section 2.5.

Equation 55 is an equation for total escape probability [6] for systems with uniform isotropic collision density. In this equation the escape probability is given for any number of pre-escape collisions and the cross sections are assumed spatially constant. Further, the escape probability of the s^{th} collided component is assumed to be spatially constant.

$$\begin{aligned}\bar{P}_{esc} &= P^0_{esc}\left[1 + (1 - P^0_{esc})\left(\frac{\sigma_s}{\sigma_t}\right) + (1 - P^0_{esc})^2\left(\frac{\sigma_s}{\sigma_t}\right)^2 + \dots\right] \\ &= \left[1 + \left(\frac{\sigma_s}{\sigma_t}\right)\frac{1 - P^0_{esc}}{P^0_{esc}}\right]^{-1}\end{aligned} \tag{55}$$

In the context of this thesis the cross sections in Equation 55 are not constant. As explained in Section 1.7.1, group averaged cross section values can be determined using Equation 16 which should be weighted by the flux distribution in energy for each successive scatter. Given the change in cross section for each collided component, the escape probability for each of the S collided components also needs to be calculated. Equation 56 is a modified version of Equation 55 which includes cross-sections that change as the photons experience collisions.

$$\begin{aligned}P^S_{esc} &= P^0_{esc} + (1 - P^0_{esc})\left(\frac{\sigma^0_s}{\sigma^0_t}\right)P^1_{esc} \\ &+(1 - P^0_{esc})(1 - P^1_{esc})\left(\frac{\sigma^0_s}{\sigma^0_t}\right)\left(\frac{\sigma^1_s}{\sigma^1_t}\right)P^2_{esc} + \dots \\ &= P^0_{esc} + \sum_{s=1}^{S}\left\{P^s_{esc}\prod_1^s(1 - P^{s-1}_{esc})\left(\frac{\sigma^{s-1}_s}{\sigma^{s-1}_t}\right)\right\}\end{aligned} \tag{56}$$

where all superscripts denote the number of collided components.

Cross sections for the s^{th} collided component are given by a one-group approximation where the energy distribution of the flux following the $s-1$ collision is

used as a weighting function. That distribution is given by Equation 57. The one-group approximation comes at no cost to the accuracy for the uncollided calculation, which is one-group due to the nature of annihilation photon production (see Section 1.3.3, on page 8).

$$\phi_g^s = \phi_{g'}^{s-1} \sigma_{g' \to g} \tag{57}$$

Using Equation 16 from Section 1.7.1, new one-group scatter and total cross sections are created for the next flight as is seen in Equations 58 and 59.

$$\sigma_s = \frac{\sum_{g'=1}^{G} \phi_{g'}^s \sigma_{s,g'}}{\sum_{g'=1}^{G} \phi_{g'}^s} \tag{58}$$

$$\sigma_t = \frac{\sum_{g'=1}^{G} \phi_{g'}^s \sigma_{t,g'}}{\sum_{g'=1}^{G} \phi_{g'}^s} \tag{59}$$

Values of P_{esc}^s for all $s > 0$ are determined by integrating over space and angle using an updated cross section given by Equation 58 for each iteration and assuming a spatially uniform distribution.

$$P_{esc}^s = \frac{\int_{x=x_{\frac{1}{2}}}^{x_{I+\frac{1}{2}}} \int_{\mu=-1}^{1} \exp(-\sigma_t^s d(\mu, x)) d\mu dx}{\int_{x=x_{\frac{1}{2}}}^{x_{I+\frac{1}{2}}} \int_{\mu=-1}^{1} d\mu dx} \tag{60}$$

Finally, a modified value of of P_{abs} is given by Equation 61 for use in Equations 51 and 52.

$$P_{abs} = 1 - P_{esc}^{S} \tag{61}$$

where P_{esc}^{S} is the total escape probability given by the sum of escape probabilities weighted by the fraction of flux remaining for each iteration as shown in Equation 62.

$$P_{esc}^{S} = \sum_{s=0}^{S} \frac{\phi^{s}}{\phi^{0}} P_{esc}^{s} \tag{62}$$

2.4 Source Definitions for Normalized Histogram Result

With the correct choice of external source definition, the histogram resulting from the deterministic method will be normalized. The choice of source depends on source location (inside or outside of the interacting medium), spatial distribution, and angular distribution. The use of unit sources is not a requirement, but eliminates the need for the normalization of resulting PHDs- which at some point need be normalized.

Inside the medium, source distributions are defined by Equation 66 . This result is evident when considering Equation 63.

$$S_{tot} = 1 = \int_{x=X_L}^{X_R} \int_{\mu=-1}^{1} S(\mu, x) d\mu dx \tag{63}$$

Assuming a uniform source distribution within any given cell and quadrature, Equation 63 discretizes to Equation 64.

$$S_{tot} = 1 = \sum_{i=1}^{I} \sum_{n=1}^{N} S_{n,i} \tag{64}$$

where

$$S_{n,i} = S(\mu_n, x_i) w_n \Delta x_i \tag{65}$$

Solving Equation 64 for the source in a given location x_{i^*} and direction μ_{n^*} gives Equation 66 for unit source definition as a function of all other source components.

$$S_{n^*,i^*} = 1 - \sum_{i=1}^{I} \sum_{n=1}^{N} (1 - \delta_{nn^*})(1 - \delta_{ii^*}) S_{n,i} \tag{66}$$

where δ is Kronecker's delta function.

In contrast to sources inside the interacting medium, sources outside of the interacting medium exist on a surface. The total source is therefore given by Equation 67, which integrates the incident angular flux on the system boundaries over all incident angles, computing the incident partial current j^-.

$$S_{tot} = 1 = \int_{\mu=0}^{1} S(\mu, X_L) \mu d\mu + \int_{\mu=-1}^{0} S(\mu, X_R) |\mu| d\mu \tag{67}$$

where X_L and X_R are the left and right boundaries of the slab, respectively.

Equation 67 discretizes to Equation 68 which is solved for $S_{\mu_{n^*}}$ in Equation 70.

$$S_{tot} = 1 = \sum_{n=1}^{N} S_n \tag{68}$$

where

$$S_n = S(\mu_n) |\mu_n| w_n \tag{69}$$

$$S_{n^*} = 1 - \sum_{n=1}^{N} (1 - \delta_{nn^*}) S_n \tag{70}$$

2.5 Annihilation Pair Source Terms

In systems where annihilation pairs are created, the source-plus-scatter term requires an additional term S_{PP}:

$$q(E, \mu, x) = \int_{-1}^{1} \int_{0}^{\infty} \psi(E', \mu', x) \sigma_s(E' \to E, \mu' \to \mu) dE' d\mu' + S_{PP}(E, \mu, x) + S_{ext}(E, \mu, x) \tag{71}$$

where

$$S_{PP}(E, \mu, x) = \int_{-1}^{1} \int_{0}^{\infty} \psi(E', \mu', x) \sigma_{PP}(E' \to E, \mu' \to \mu) Y_{PP} dE' d\mu' \tag{72}$$

and Y_{PP} is the yield of annihilation photons.

The additional source term S_{PP} accounts for the creation of positron-electron pairs. The range and time-frame of the interaction of these pairs is exceedingly small, such that we can treat them as an equivalent source of annihilation photons . The cross section in the additional source term (Equation 72) is separable in angle and energy:

$$\sigma_{PP}(E' \to E, \mu' \to \mu) = \sigma_{PP}(E' \to E) P_{PP}(\mu' \to \mu) \tag{73}$$

The separation in Equation 73 is possible due to independence of energy and direction of annihilation photons. Because positrons lose most of their kinetic energy

before annihilating with an electron, we can take the probability of annihilation photon creation at energy E as a delta function at the energy equivalent to half the positron-electron rest mass (0.511 MeV). The probability of photons undergoing pair production below 1.022 MeV is zero due to the energy threshold for the reaction:

$$\begin{gathered}\sigma_{PP}(E' \rightarrow E) = 0, \\ E' < 1.022\text{MeV} \\ \text{or} \\ E \neq \frac{2m_0c^2}{2} = 0.511\text{MeV}\end{gathered} \tag{74}$$

Due to the isotropic nature of annihilation photon generation, $\sigma_{PP}(\mu' \rightarrow \mu)$ is given by:

$$P_{PP}(\mu' \rightarrow \mu) = \frac{\int_{-1}^{1} P_{PP}(\mu' \rightarrow \mu)d\mu}{\int_{-1}^{1} d\mu} = \frac{1}{2} \tag{75}$$

Substituting the preceding simplifications into Equation 72 yields Equation 76 for the annihilation pair source term.

$$\begin{aligned}S_{PP}(0.511\text{ MeV}, \mu, x) &= \int_{-1}^{1}\int_{1.022\text{ MeV}}^{\infty} \psi(E', \mu', x)\frac{1}{2}\sigma_{PP}(E')(2^*)dE'd\mu' \\ &= (2^*)\frac{1}{2}\int_{1.022\text{ MeV}}^{\infty} \phi(E', x)\sigma_{PP}(E')dE'\end{aligned} \tag{76}$$

The yield (2^*) is written with an asterisk to draw attention to the distinction

between determining a source of individual annihilation photons or annihilation pairs (a yield of 2 or 1, respectively).

Discretized values of the annihilation source are given by Equation 77 which integrates the source over space and angle group boundaries. Due to energy discretization, annihilation photons cannot be sourced at exactly 0.511 MeV. Instead they are distributed over the energy group g^* which bounds 0.511 MeV. Similarly, g^{**} is defined as the group bounding 1.022 MeV.

$$\begin{aligned} S_{PP,g^*,n,i} &= \frac{1}{2} \int_{x_{i-\frac{1}{2}}}^{x_{i+\frac{1}{2}}} \int_{\mu_{n-\frac{1}{2}}}^{\mu_{n+\frac{1}{2}}} S_{PP}(\mu, x) d\mu dx \\ &= \frac{\Delta\mu_n}{2} \sum_{g'=g^{**}}^{E_{G'}} \phi_{g',i} \sigma_{PP,g'} \end{aligned} \tag{77}$$

2.6 Incident Energy – Annihilation Source Correlation

To accurately simulate a PHD in a system with pair production it will be necessary to correlate annihilation pair source terms with incident radiation energy E^S. There are two elements to the correlation. The first is determining the fraction of flux at energy E' that entered the system at energy E^S. The second is determining the fraction of the annihilation pair source term that was created by flux at energy E'.

A method for determining the fraction of flux at energy E' that entered the system at energy E^S has already be established by Benz and was discussed in Section 1.8. In the context of Section 1.8 the equations track the fraction of j^+ escaping the system at energy E that entered the system at energy E^S. Its

application here is analogous, as photons lost to pair production are also leaving the system.

To determine the fraction of the annihilation-pair source term that was created by flux at energy E' we will restrict the range of E' in Equation 76 to a set of discrete values that correspond to the energy bins used in the primary transport.

$$S_{PP,g'\to g^*,n,i} = \frac{1}{2}\int_{x_{i-\frac{1}{2}}}^{x_{i+\frac{1}{2}}}\int_{\mu_{n-\frac{1}{2}}}^{\mu_{n+\frac{1}{2}}}\int_{E_{g'+\frac{1}{2}}}^{E_{g'-\frac{1}{2}}} \phi(E',x)\sigma_{PP}(E')dE'd\mu dx$$

$$= \frac{w_n\mu_n}{2}\phi_{g',i}\sigma_{PP:g'} \tag{78}$$

where

$$E_{g'-\frac{1}{2}} \;\geq\; E_{g^{**}}$$

Collecting all annihilation pairs in cell i that are caused by incident external source group g^S is accomplished by summing the fraction of the annihilation source in each group g' that resulted from group g^S– as is seen in Equation 79.

$$S_{PP,g^S,i} = \sum_{g'=g^{**}}^{g^S} f_{g^S\to g'}\frac{w_n\mu}{2}\phi_{g',i}\sigma_{PP:g'} \tag{79}$$

2.7 Complete PHD

2.7.1 Opposing-Ordinate Combination Solutions

Integrating the product of the distribution created in Equation 49 and the pair production source term given by Equation 77 over the system dimensions creates an effective pulse height distribution for annihilation photons system-wide (511-Pair PHD). That distribution can then be combined with the primary PHD (P^{-PP}) to create the complete PHD ($\mathbf{P}$). This combination is shown in Equations 80 and 81.

$$\mathbf{P}(E^S - 1.022 + E^{\xi'}) = P^{-PP}(E^S - 1.022 + E^{\xi'}) + \int_{x=0}^{L} S^{PP}(E^S, x)\bar{P}(E^{\xi'}, x)dx \quad (80)$$

where $\bar{P}(E^{\xi'}, x)$ is the effective PHD for annihilation photons generated at x defined in Section 2.2.2.

Discrete values of $\mathbf{P}$ are given by Equation 81.

$$\mathbf{P}_{h''} = P^{-PP}_{h''} + \sum_{i=1}^{I} S_{PP,g^S,i}\bar{P}_{h',i} \quad (81)$$

Due to the 1.022 MeV shift, the primary bins may not coincide with the 511-Pair bins– requiring the values to be distributed appropriately.

The energy boundaries for the bins associated with the PHD of the 511-Pair, shifted from the group of the incident source which created them, is given by Equation 82. This is the bin structure defined by Equation 47 shifted by the discretized range of $E' - 1.022$.

$$\begin{aligned} E^{\xi}_{h''_{-\frac{1}{2}}} &= E_{g'+\frac{1}{2}} - 1.022 + E^{\xi}_{h'_{-\frac{1}{2}}} \\ E^{\xi}_{h''_{+\frac{1}{2}}} &= E_{g'-\frac{1}{2}} - 1.022 + E^{\xi}_{h'_{+\frac{1}{2}}} \end{aligned} \quad (82)$$

where

$E^{\xi}_{h''_{\pm\frac{1}{2}}} \equiv$ energy bounds for indices of the shifted 511-Pair PHD group structure

$E^{\xi}_{h'\pm\frac{1}{2}} \equiv$ energy bounds for indices of the 511-Pair PHD group structure defined by Equation 47

2.7.2 Modified First-Flight Approximation Solutions

Peaks created using the modified first-flight method are distributed in a manner similar to those created using OOC. In Equation 81, the $\bar{P}_{h',i}$ distribution is replaced with the probabilities calculated in Equations 50-52. The products of the cell-specific annihilation photon source and escape probability are combined with the primary distribution ($P^{-PP}_{h''}$) according to Equation 83.

$$\mathbf{P}_{h''} = \begin{cases} P^{-PP}_{h''} + \sum_{i=1}^{I} S_{PP,g^S,i} P_{DE,i} & \text{, double escape peak} \\ P^{-PP}_{h''} + \sum_{i=1}^{I} S_{PP,g^S,i} P_{SE,i} & \text{, single escape peak} \\ P^{-PP}_{h''} + \sum_{i=1}^{I} S_{PP,g^S,i} P_{ZE,i} & \text{, zero escape peak} \\ P^{-PP}_{h''} & \text{, otherwise} \end{cases} \tag{83}$$

The bin boundaries for the double, single, and zero escape peaks of Equation 83 may not coincide with the boundaries for $P^{-PP}_{h''}$. The DE, SE, and ZE contributions need to be distributed proportionally into the following h'' bins:

Double Escape Peak

h'' where $E^{\xi}_{h''\pm\frac{1}{2}}$ is on the interval $[E_{g^S+\frac{1}{2}} - 1.022\text{MeV}, E_{g^S-\frac{1}{2}} - 1.022\text{MeV}]$

Single Escape Peak

h'' where $E^{\xi}_{h''\pm\frac{1}{2}}$ is on the interval $[E_{g^S+\frac{1}{2}} - 0.511\text{MeV}, E_{g^S-\frac{1}{2}} - 0.511\text{MeV}]$

Zero Escape Peak

h'' where $E^{\xi}_{h''\pm\frac{1}{2}}$ is on the interval $[E_{g^S+\frac{1}{2}}, E_{g^S-\frac{1}{2}}]$

[**Note**: g^S is the group index of the flux creating the annihilation photon source.]

2.8 Energy Deposition Distributions for Group-to-Group Transfer

The energy bounds for ΔN in the previous work by Benz and Palmer were given by Equation 84 [1]:

$$\begin{aligned} E^{\xi}_{min} &= E_{g'+\frac{1}{2}} - E_{g-\frac{1}{2}} \\ E^{\xi}_{max} &= E_{g'-\frac{1}{2}} - E_{g+\frac{1}{2}} \end{aligned} \tag{84}$$

Equations 84 result in a width for energy deposition bin h given by $\Delta E^{\xi}_{h} = \Delta E_{g'} + \Delta E_{g}$. A histogram created using this bin structure will accurately tally deposition events independent of the flux distributions within g' and g. However, if the flux distribution is uniform within the bins, higher resolution can be obtained.

We have considered the distribution of deposition events within these energy bounds. We assume that particles are equally like to have any energy within a group g' and, in the case of downscatter, scatter uniformly to any energy within group g. This assumption will be valid in most cases because the multigroup energy structure was chosen to limit within-group variation in the flux profile (as was required to generate multi-group cross sections without a priori knowledge of the flux profile).

In the case of within-group scatter, similar assumptions are made: particles are equally likely scatter from any energy within group g' and to another energy within the same group ($g = g'$) *below* the originating energy.

For absorption events, particles are assumed to have any energy within a group g' with equal probability and arrive at exactly zero energy.

Given these assumptions, the distributions of energy deposition events can be predicted with Equations 85, 86 and 87 for inscatter, downscatter, and absorption

respectively.

Inscatter $(g' = g)$

$$P(E^\xi) = \int_{E'_{min}(E^\xi)}^{E'_{max}(E^\xi)} \frac{1}{\Delta E_{g'}} \frac{1}{E' - E_{g+\frac{1}{2}}} dE' \tag{85}$$
$$= \begin{cases} \frac{\ln(\Delta E_{g'}) - \ln(E^\xi)}{\Delta E_{g'}}, & 0 < \quad E^\xi \quad \leq \Delta E_{g'} \\ 0, & \text{otherwise.} \end{cases}$$

Downscatter $(g' < g)$

$$P(E^\xi) = \int_{E'_{min}(E^\xi)}^{E'_{max}(E^\xi)} \frac{1}{\Delta E_{g'}} \frac{1}{\Delta E_g} dE' \tag{86}$$
$$= \begin{cases} \frac{E^\xi - (E_{g'+\frac{1}{2}} - E_{g-\frac{1}{2}})}{\Delta E_{g'} \Delta E_g}, & E_{g'+\frac{1}{2}} - E_{g-\frac{1}{2}} \leq \quad E^\xi \quad \leq E_{g'} - E_g \\ \frac{(E_{g'-\frac{1}{2}} - E_{g+\frac{1}{2}}) - E^\xi}{\Delta E_{g'} \Delta E_g}, & E_{g'} - E_g \leq \quad E^\xi \quad \leq E_{g'-\frac{1}{2}} - E_{g+\frac{1}{2}} \\ 0, & \text{otherwise.} \end{cases}$$

Absorption

$$P(E^\xi) = \begin{cases} \frac{1}{\Delta E_{g'}}, & E_{g'+\frac{1}{2}} \leq \quad E^\xi \leq \quad E_{g'-\frac{1}{2}} \\ 0, & \text{otherwise.} \end{cases} \tag{87}$$

The bounds of the integrals in Equations 85 and 86 that limit integration to portions of group g' from which scatter can result in an energy deposition E^ξ while staying in the bounds of group g are given by Equations 88-89.

Inscatter $(g' = g)$

$$E'_{max} = E_{g'-\frac{1}{2}}$$
$$E'_{min} = E_{g'+\frac{1}{2}} + E^\xi \tag{88}$$

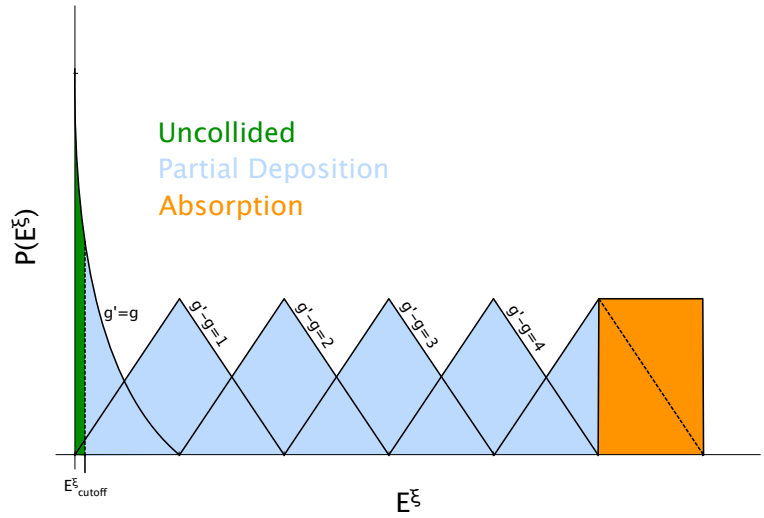

Figure 7: Representation of energy deposition probabilities as a function of group index change and deposition energy.

Downscatter $(g' < g)$

$$E'_{max} = E_{g'+\frac{1}{2}} + \frac{E^{\xi}}{2} - \frac{1}{2}(E_{g'+\frac{1}{2}} - E_{g-\frac{1}{2}})$$

$$E'_{min} = E_{g'+\frac{1}{2}}$$

and (89)

$$E'_{max} = E_{g'-\frac{1}{2}}$$

$$E'_{min} = E_{g'-\frac{1}{2}} - \frac{1}{2}(E_{g'-\frac{1}{2}} - E_{g+\frac{1}{2}}) - \frac{E^{\xi}}{2}$$

Figure 7 shows the distributions created with Equations 85-87. The down-scatter distributions will be referred to as "triangular" in this thesis due to their triangular shape. The region of the within-group scatter distribution below E^{ξ}_{cutoff} shown in green is the fraction of uncollided flux and is given by the integration of Equation 85 between E^{ξ}_{cutoff} and zero.

3 Results

3.1 Introduction

We being by presenting results of the new energy deposition distributions introduced in Section 2.8. We will then present information related to the separation of annihilation photons from the aggregate transfer cross sections to demonstrate effective separation of annihilation photons from the calculations of "primary" PHDs. Next, results needed to evaluate the accuracy and efficiency of single, double, and zero escape peak area calculations using both opposing-ordinate PHD combination (OOC) and the modified first-flight approximation (MFF) will be presented. These results will be presented in conjunction with distributions and peak area estimates created using MCNP5 that serve as a benchmark for comparison. All OOC and MFF test problem results are based on mono-energetic sources of 1.6 MeV or 2.6 MeV photons incident on slabs of several thicknesses. Lastly, the results of an interaction parameter study are presented. The purpose of the iteration parameter study was to determine the number of scattered component iterations needed to converge transport solutions for spatially uniform, isotropic 0.511 MeV sources in slab geometry.

3.2 Energy Deposition Distributions for Group-to-Group Transfer

In this section we show results from the new approach to deposition energy distributions and bin structuring discussed in Section 2.8.

3.2.1 Within-group Scatter

The first set of data, shown in Table 2, gives estimates of uncollided flux ($\phi_{uncollided}$) based on different values of E^{ξ}_{cutoff}. [See the end of Section 2.8 for discussion on the

relationship between E^{ξ}_{cutoff} and the uncollided flux.] The independent variable, E^{ξ}_{cutoff}, is given as a ratio of its value to the total within-group scatter bin width.

Uncollided Flux Estimates ($\phi_{uncollided}$)				
Mat.	$\frac{E^{\xi}_{co}}{\Delta E^{\xi}_{h}}$	**Determ.**	**MCNP**	**rel. err.**
Ge	0.1	9.9838E-02	3.0239E-01	0.0005
	0.2	1.6086E-01	3.0268E-01	0.0005
	0.4	2.3200E-01	3.0331E-01	0.0005
	0.6	2.7458E-01	3.0393E-01	0.0005
	0.9	3.0173E-01	3.0493E-01	0.0005
	1.0	3.0180E-01		
NaI	0.1	1.4325E-01	4.3708E-01	0.0004
	0.2	2.3076E-01	4.3735E-01	0.0004
	0.4	3.3274E-01	4.3794E-01	0.0004
	0.6	3.9370E-01	4.3855E-01	0.0004
	0.9	4.3244E-01	4.3946E-01	0.0004
	1.0	4.3330E-01		
Pb	0.1	2.0425E-02	6.1169E-02	0.0012
	0.2	3.2920E-02	6.1256E-02	0.0012
	0.4	4.7513E-02	6.1474E-02	0.0012
	0.6	5.6270E-02	6.1696E-02	0.0012
	0.9	6.1905E-02	6.2049E-02	0.0012
	1.0	6.1700E-02		

Table 2: Uncollided flux estimates for 1.6 MeV photons normally ($\mu = 0.997$) incident on 5 cm thick slabs of germanium, sodium iodide, and lead with respective material densities of ρ=5.323 g/cm^3, ρ=3.67 g/cm^3 (15 wt.% Na, 85 wt.% I), and ρ=11.34 g/cm^3. In all cases Sn 32 quadrature, 100 energy groups, and 1cm cells were used except for lead which had 0.5cm cells.

3.2.2 Downscatter

Table 3 gives the difference between deterministic and MCNP5 estimates averaged over all deposition bins resulting from downscatter. The average values were determined using Equation 90. These values are included as a metric for the effectiveness of the proposed downscatter energy deposition distribution discussed in Section 2.8.

$$\text{Avg. \% Diff.} = \frac{\sum_{h=1}^{H} \frac{\left| \frac{\Delta N_{h,MCNP5}}{\Delta E_h} - \frac{\Delta N_{h,Determ.}}{\Delta E_h} \right|}{\frac{\Delta N_{h,MCNP5}}{\Delta E_h}}}{H} * 100\% \tag{90}$$

Bins containing greater than 200 % error were excluded from the calculation. It was assumed that those errors are due to differences in multigroup and continuous transport and therefore skew the comparison.

Average Bin Estimate Comparision – Avg. % Diff.		
Mat.	Uniform	Triangular
Ge	6.74082E+00	4.60425E+00
NaI	7.70413E+00	7.21813E+00
Pb	1.07157E+01	9.23082E+00

Table 3: Average percent difference between deterministic and MCNP5 estimates for 1.6 MeV photons normally ($\mu = 0.997$) incident on 5 cm thick slabs of germanium, sodium iodide, and lead with respective material densities of ρ=5.323 g/cm^3, ρ=3.67 g/cm^3 (15 wt.% Na, 85 wt.% I), and ρ=11.34 g/cm^3. In all cases $S_3 2$ quadrature, 100 energy groups, and 1 cm cells were used except for lead which had 0.5 cm cells.

Figures 8-10 compare distributions of the aforementioned simulations comparing results based on the deposition energy distributions suggested in Section 2.8 to results given by the uniform energy deposition distributions presented by Benz and Palmer [1].

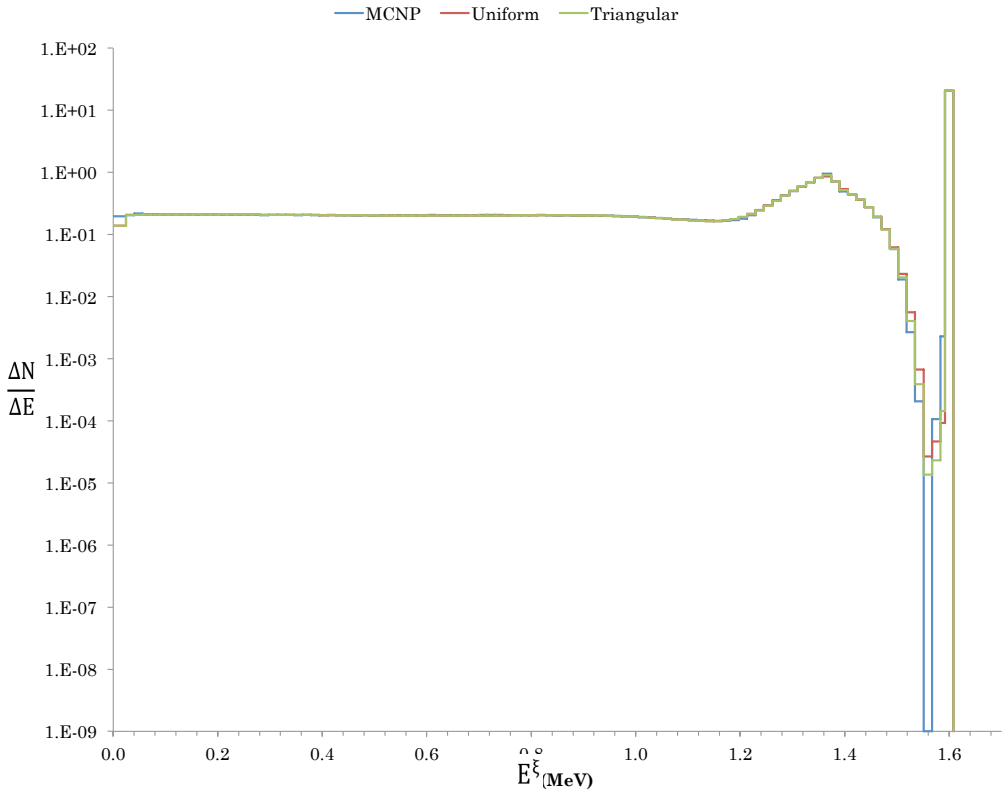

Figure 8: Pulse height distributions from 1.6 MeV photons normally ($\mu = 0.997$) incident on a 5 cm thick germanium slab using MCNP5 and the deterministic method with uniform and triangular energy deposition distributions. All pair production events treated as full energy depositions. ρ=5.323 g/cm^3

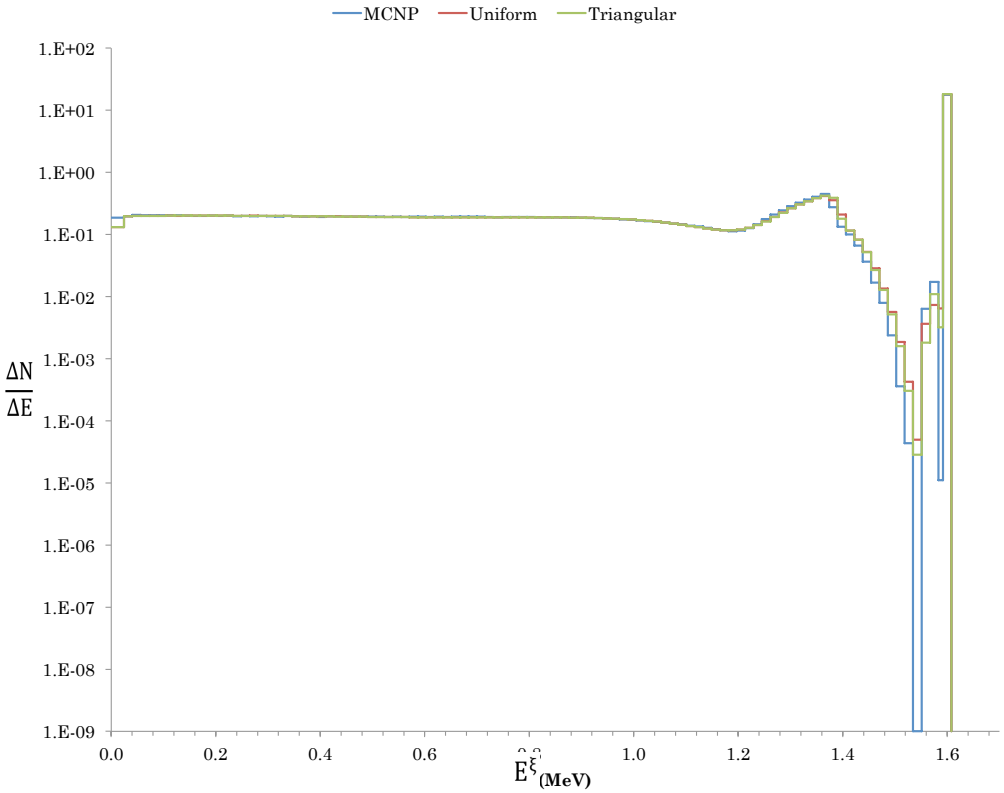

Figure 9: Pulse height distributions from 1.6 MeV photons normally ($\mu = 0.997$) incident on a 5 cm sodium iodide slab using MCNP5 and the deterministic method with uniform and triangular energy deposition distributions. All pair production events treated as full energy depositions. ρ=3.67 g/cm^3 (15 wt.% Na, 85 wt.% I)

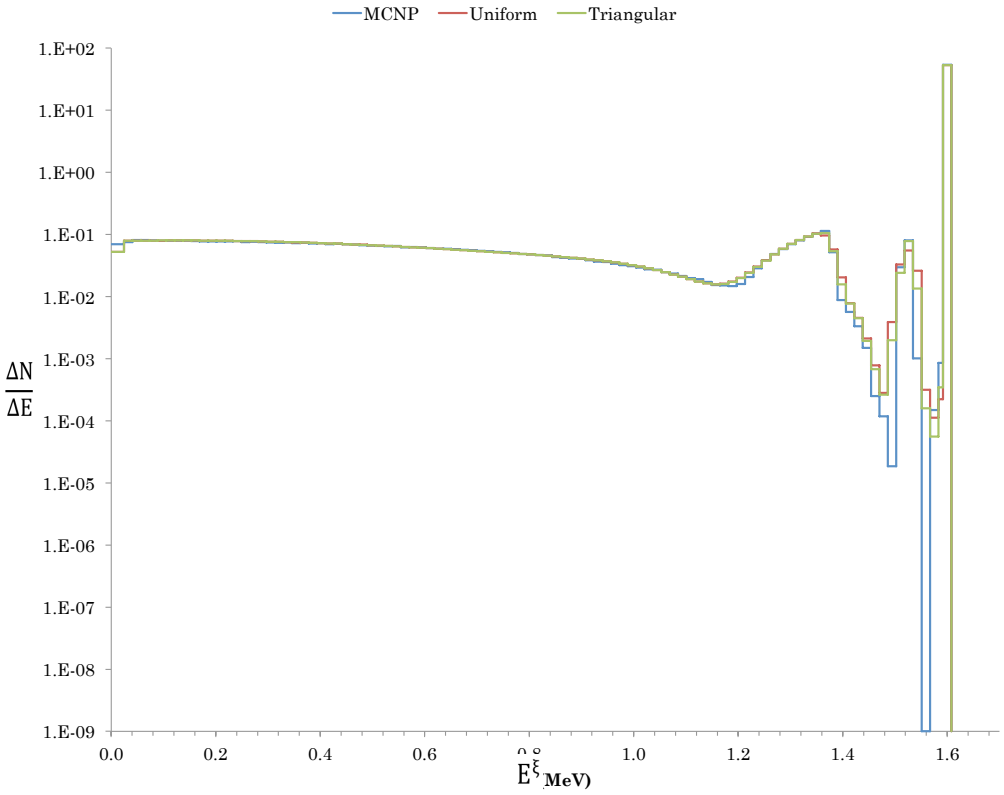

Figure 10: Pulse height distributions from 1.6 MeV photons normally ($\mu = 0.997$) incident on a 5 cm lead slab using MCNP5 and the deterministic method with uniform and triangular energy deposition distributions. All pair production events treated as full energy depositions. ρ=11.34 g/cm^3

3.3 Separation of Annihilation Photons From Transfer Cross Sections

Figure 11 is a three-dimensional graph of an aggregate transfer cross section set which includes annihilation photon production. The specific cross sections which include the source of 0.511 MeV photons are shown in orange. It is included as a visual aid to understanding how the source of annihilation photons was isolated in this research.

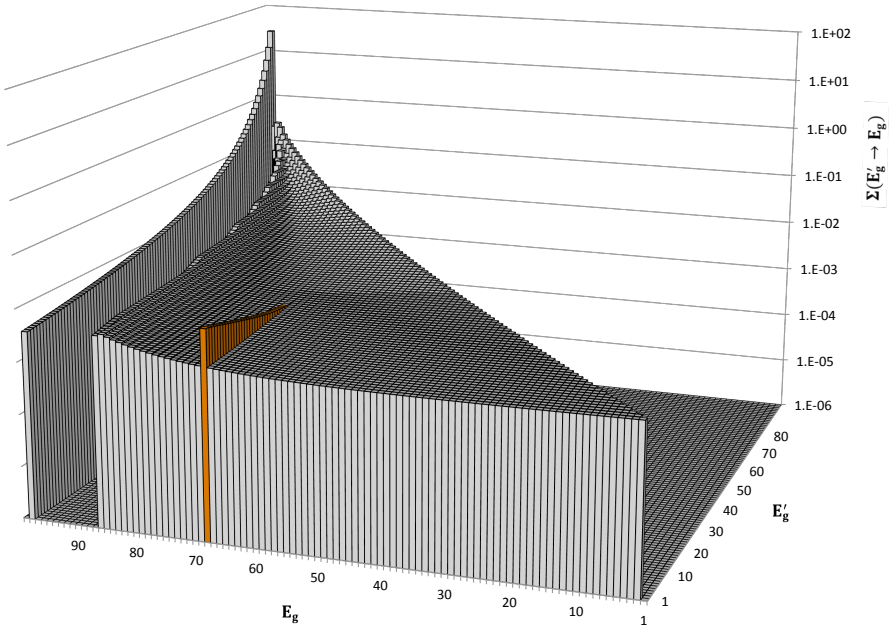

Figure 11: 100-group transfer cross sections for NaI. Average energy of first group is 1.6 MeV. Annihilation photon production seen in orange at approximately E_{70} from each E'_g above threshold.

Figures 12 - 14 show "primary" PHDs generated deterministically and with MCNP5 using equivalent bin structure. In these PHDs, annihilation photons were removed from downscatter and pair production was treated as absorption in both the deterministic and MCNP5 calculations. The deterministic and MCNP5 PHDs are labeled "Determ.-PP" and "MCNP-PP" respectively with "-PP" indicating that the effects of pair production are not treated thoroughly in the distributions. These figures have been included to demonstrate how effectively the annihilation photon source was removed from the downscatter matrix. A sample MCNP5 input

used to generate this data can be found in Appendix B. The deterministic transport simulations used the S_{32} angular quadrature, 5 uniform spatial cells and 10 scattered components of the flux.

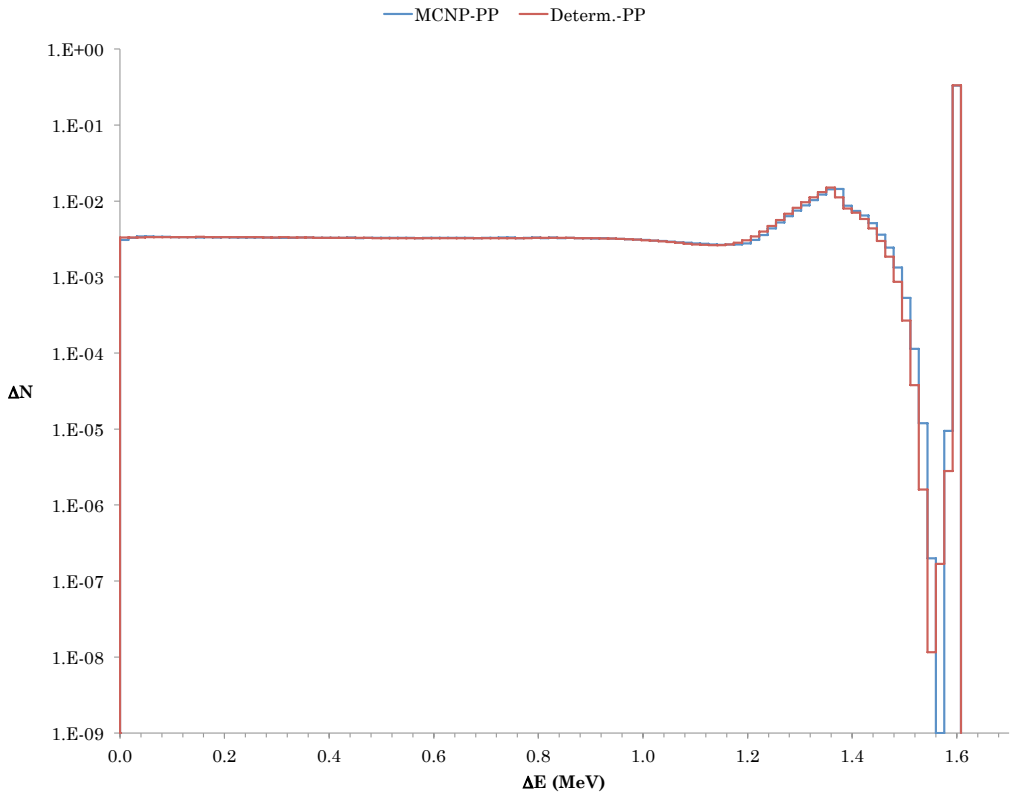

Figure 12: Pulse height distributions from 1.6 MeV photons normally ($\mu = 0.997$) incident on a 5 cm thick germanium slab using MCNP5 and the deterministic method, where all annihilation pairs are assumed fully absorbed. ρ=5.323 g/cm^3

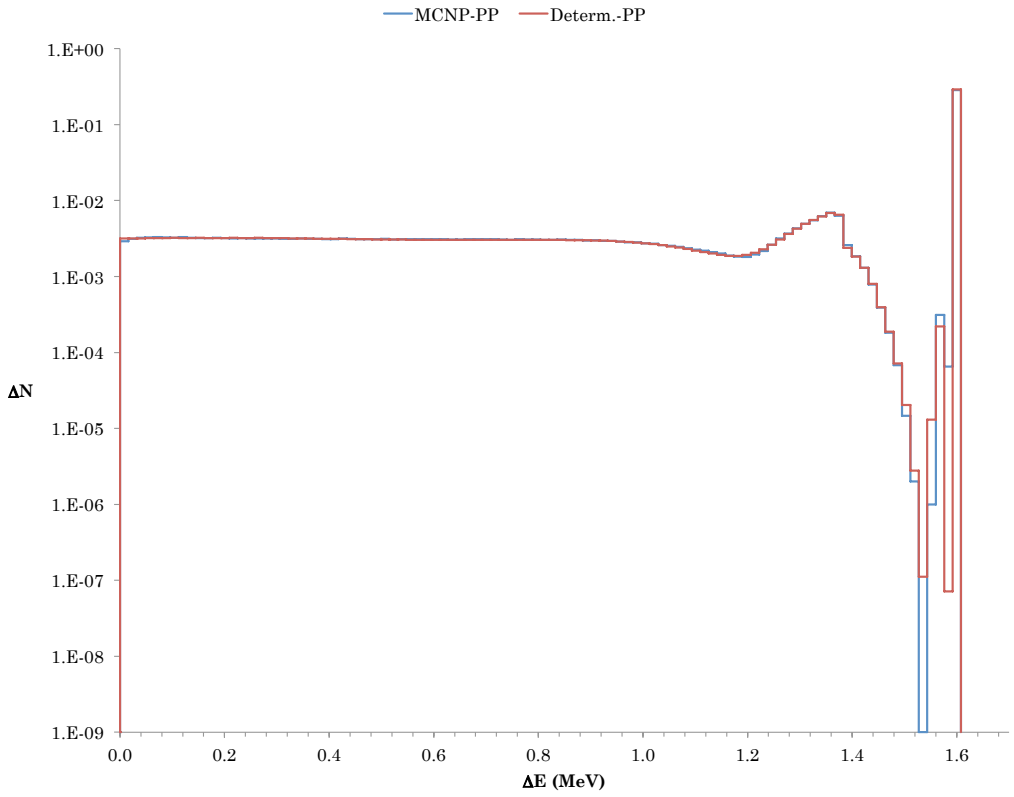

Figure 13: Pulse height distributions from 1.6 MeV photons normally ($\mu = 0.997$) incident on a 5 cm sodium iodide slab using MCNP5 and the deterministic method, where all annihilation pairs are assumed fully absorbed. ρ=3.67 g/cm^3 (15 wt.% Na, 85 wt.% I)

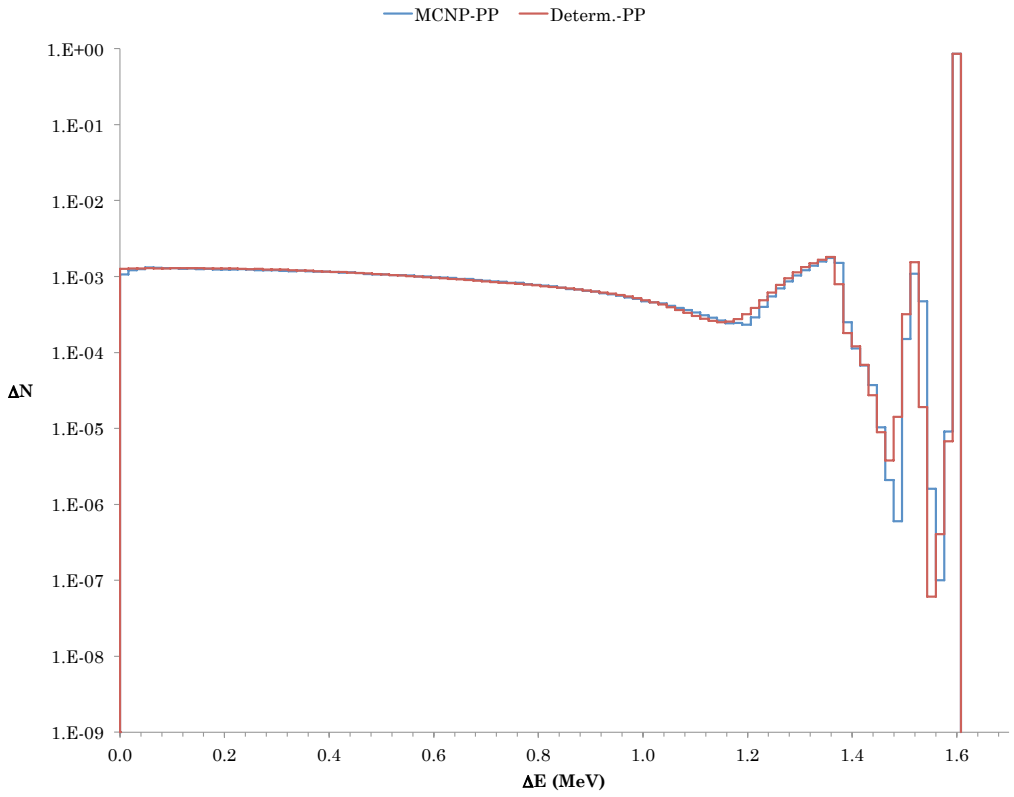

Figure 14: Pulse height distributions from 1.6 MeV photons normally ($\mu = 0.997$) incident on a 5 cm lead slab using MCNP5 and the deterministic method where, all annihilation pairs are assumed fully absorbed. ρ=11.34 g/cm^3

3.4 Opposing-Ordinate PHD Combination Method

Figures 15-26 show the results of the opposing-ordinate PHD combination (OOC) simulations. They are compared against MCNP5 PHDs with matching bin structure. These figures are included to provide a qualitative comparison of OOC results with those given by MCNP5. The deterministic PHD series and MCNP5 series are labeled "Determ.+PP" and "MCNP+PP" respectively with "+PP" indicating that the effects of pair production are included in the distributions. All deterministic

transport simulations used the S_{32} angular quadrature, 5 uniform spatial cells, and 10 scattered components of the flux.

The same data are presented in Tables 4 and 5 on pages 74 and 75, where values are given for the area under the single, double and zero escape peaks and the percentage difference between the OOC and MCNP5 results. The percent difference, labeled % Diff, is given by:

$$\%\text{Diff} = \frac{\text{MCNP5} - \text{Determ.}}{\text{MCNP5}} \tag{91}$$

where MCNP5 and Determ. are the area estimates of a given peak.

Both 1.6 and 2.6 MeV source photons were used to demonstrate the ability to use a system-specific, effective annihilation photon PHD in conjunction with different source-specific annihilation photon source terms. The same system-specific, effective annihilation photon PHDs (which are based on system geometry and composition only) were used in the respective deterministic PHDs in this section.

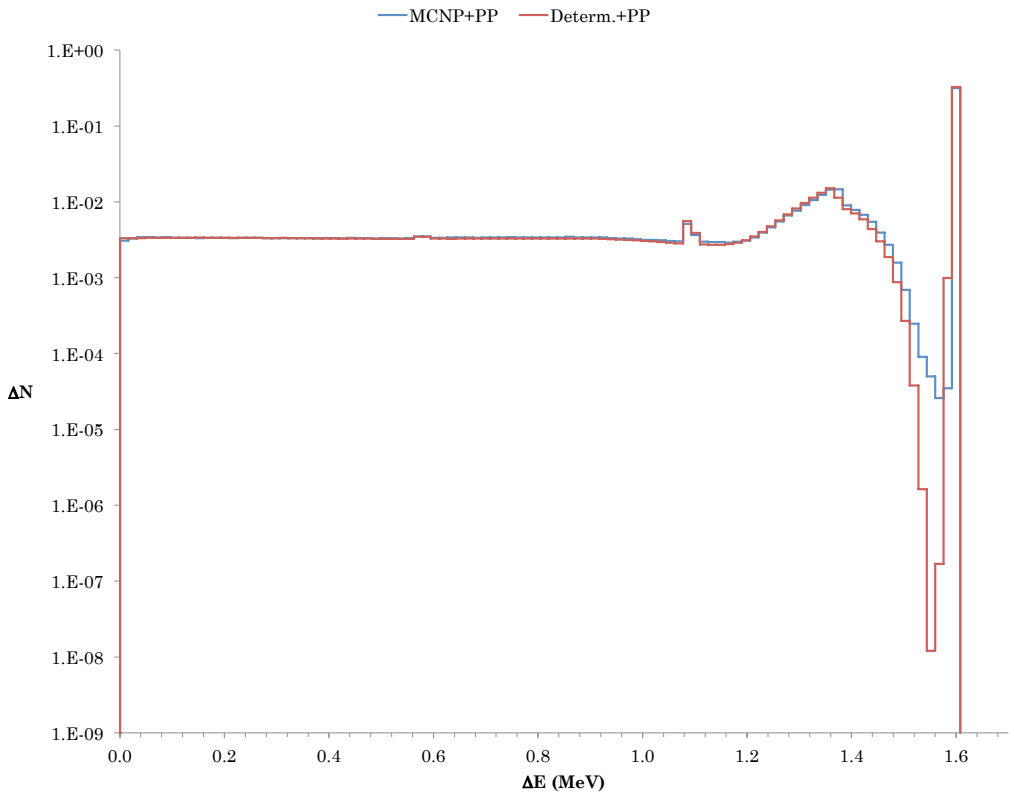

Figure 15: Pulse height distributions from 1.6 MeV photons normally ($\mu = 0.997$) incident on a 5 cm thick germanium slab using the OOC pair production treatment and MCNP5. ρ=5.323 g/cm^3

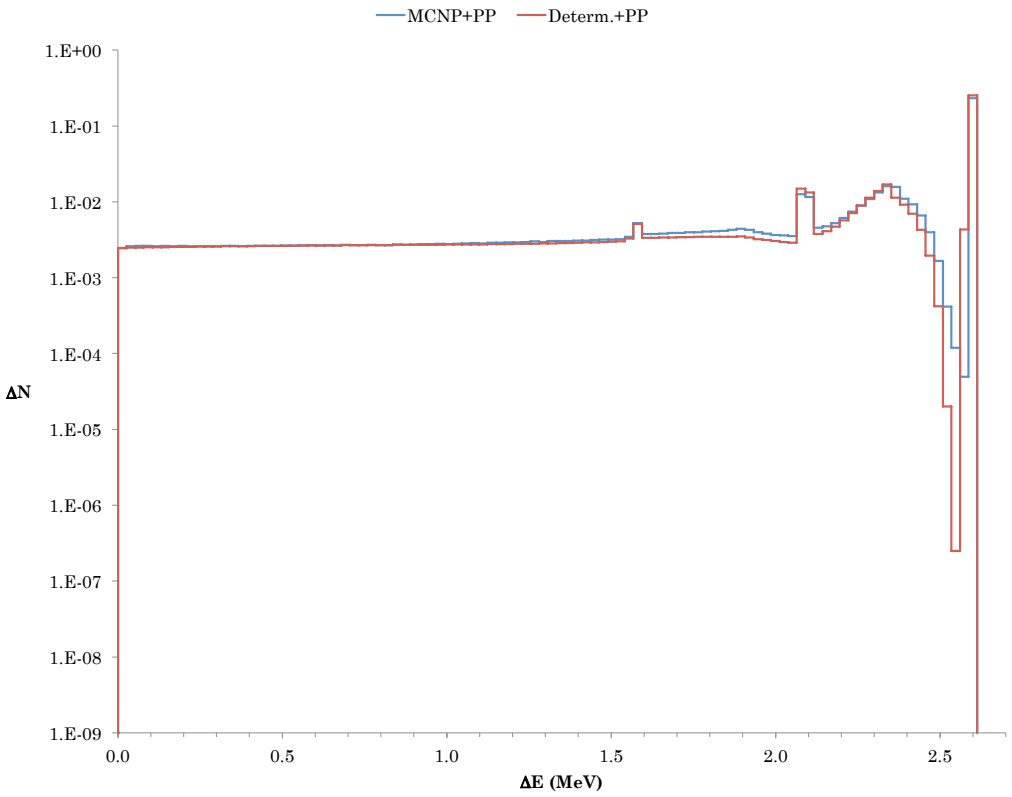

Figure 16: Pulse height distributions from 2.6 MeV photons normally ($\mu = 0.997$) incident on a 5cm thick germanium slab using the OOC pair production treatment and MCNP5. ρ=5.323 g/cm^3

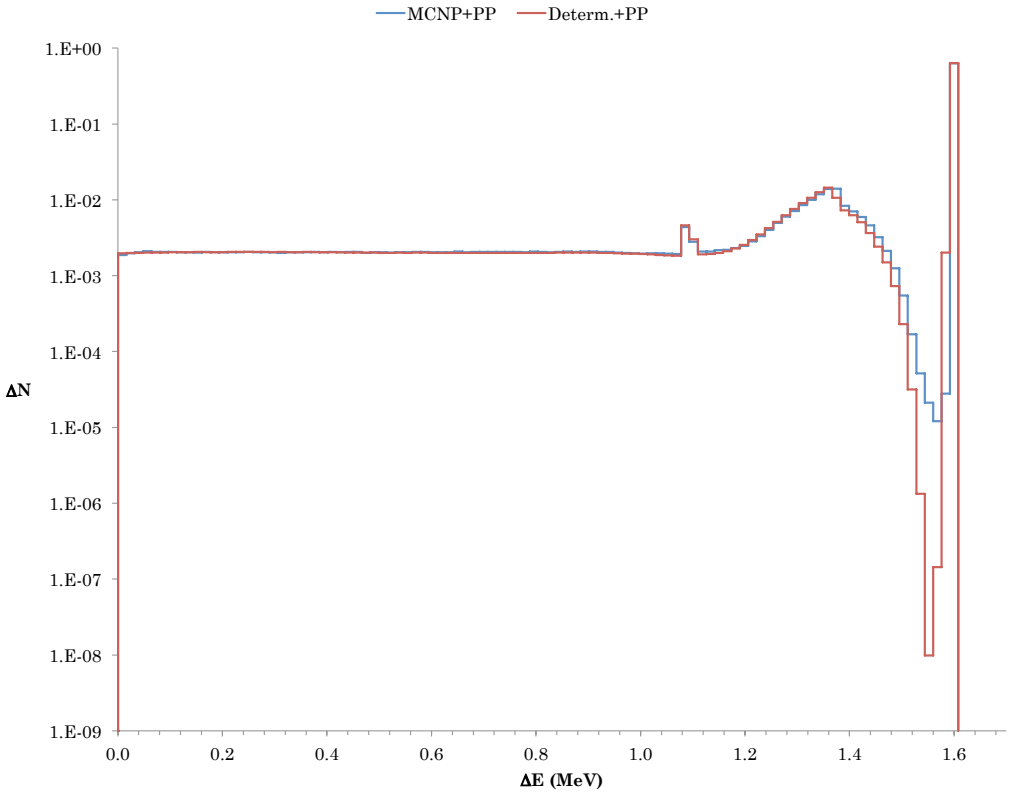

Figure 17: Pulse height distributions from 1.6 MeV photons normally ($\mu = 0.997$) incident on a 10 cm thick germanium slab using the OOC pair production treatment and MCNP5. ρ=5.323 g/cm^3

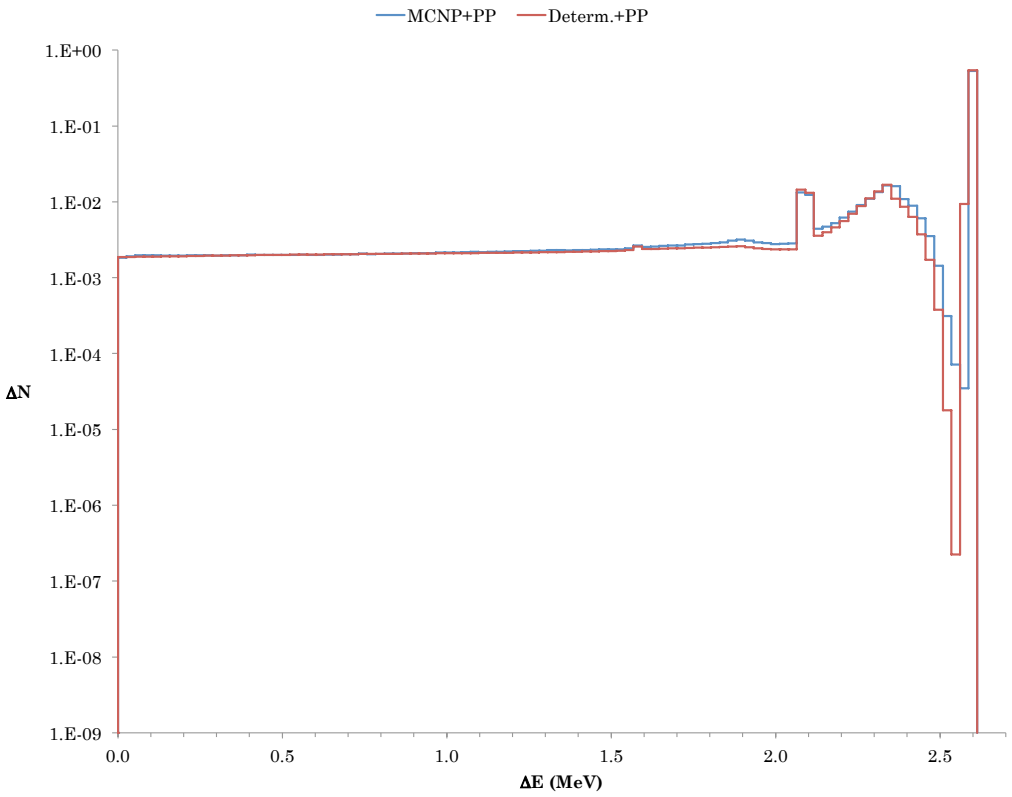

Figure 18: Pulse height distributions from 2.6 MeV photons normally ($\mu = 0.997$) incident on a 10 cm thick germanium slab using the OOC pair production treatment and MCNP5. ρ=5.323 g/cm^3

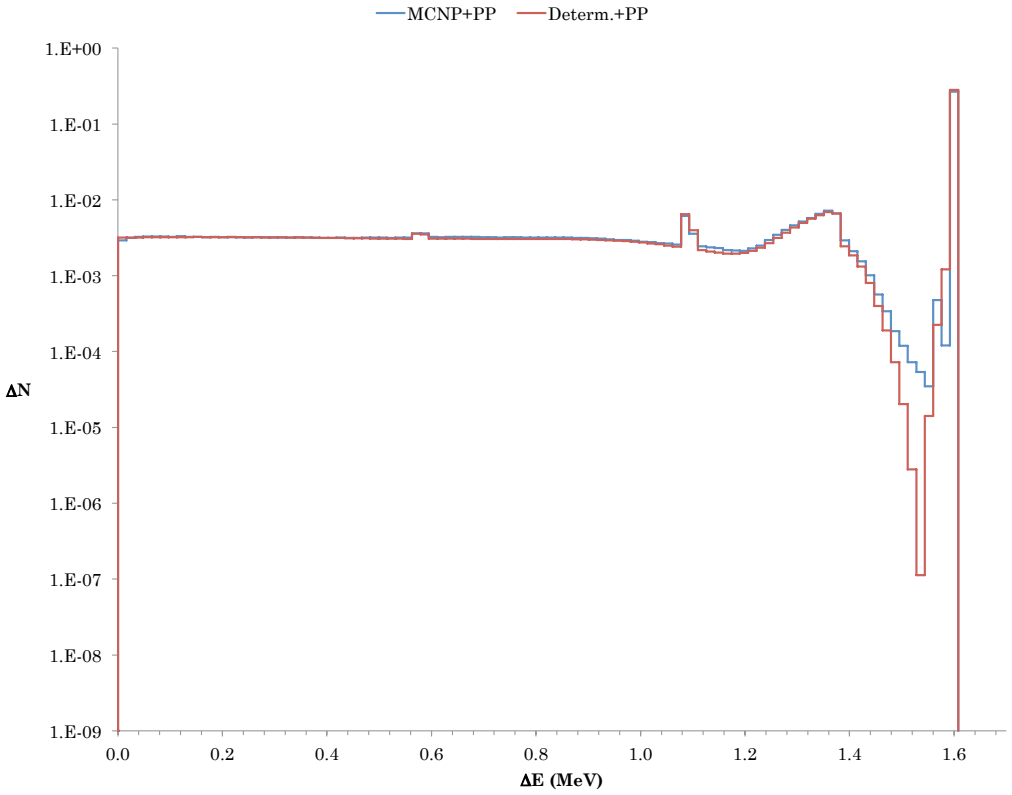

Figure 19: Pulse height distributions from 1.6 MeV photons normally ($\mu = 0.997$) incident on a 5 cm thick sodium iodide slab using the OOC pair production treatment and MCNP5. ρ=3.67 g/cm^3 (15 wt.% Na, 85 wt.% I)

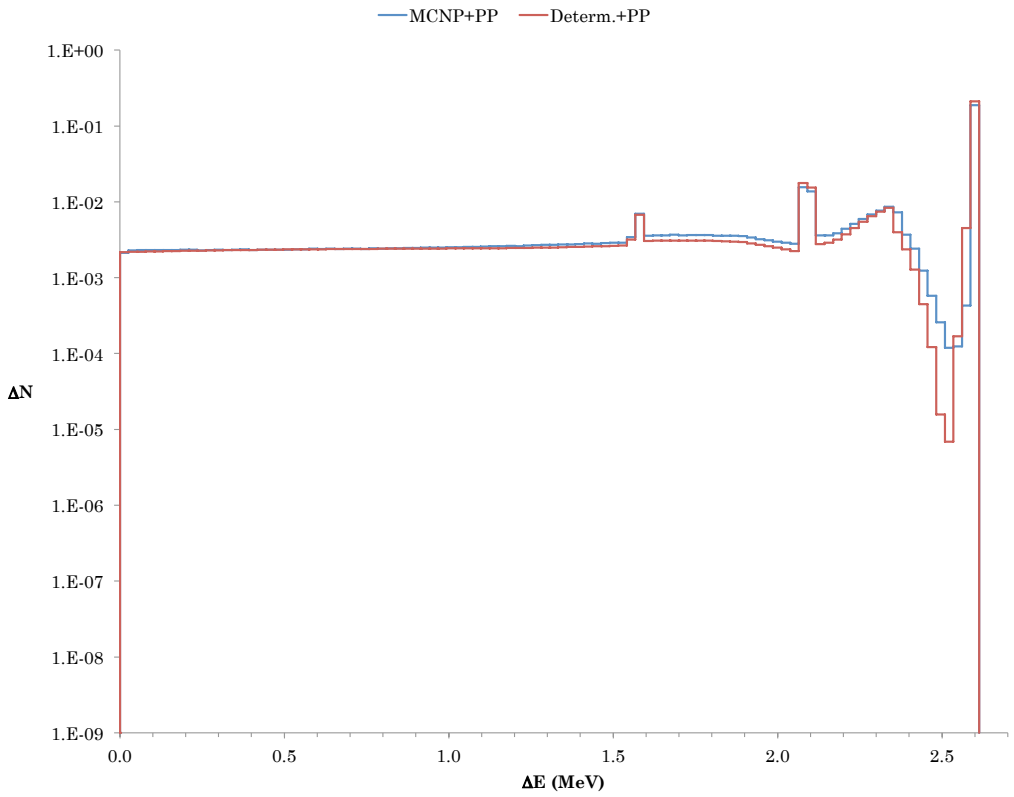

Figure 20: Pulse height distributions from 2.6 MeV photons normally ($\mu = 0.997$) incident on a 5 cm thick sodium iodide slab using the OOC pair production treatment and MCNP5. ρ=3.67 g/cm^3 (15 wt.% Na, 85 wt.% I)

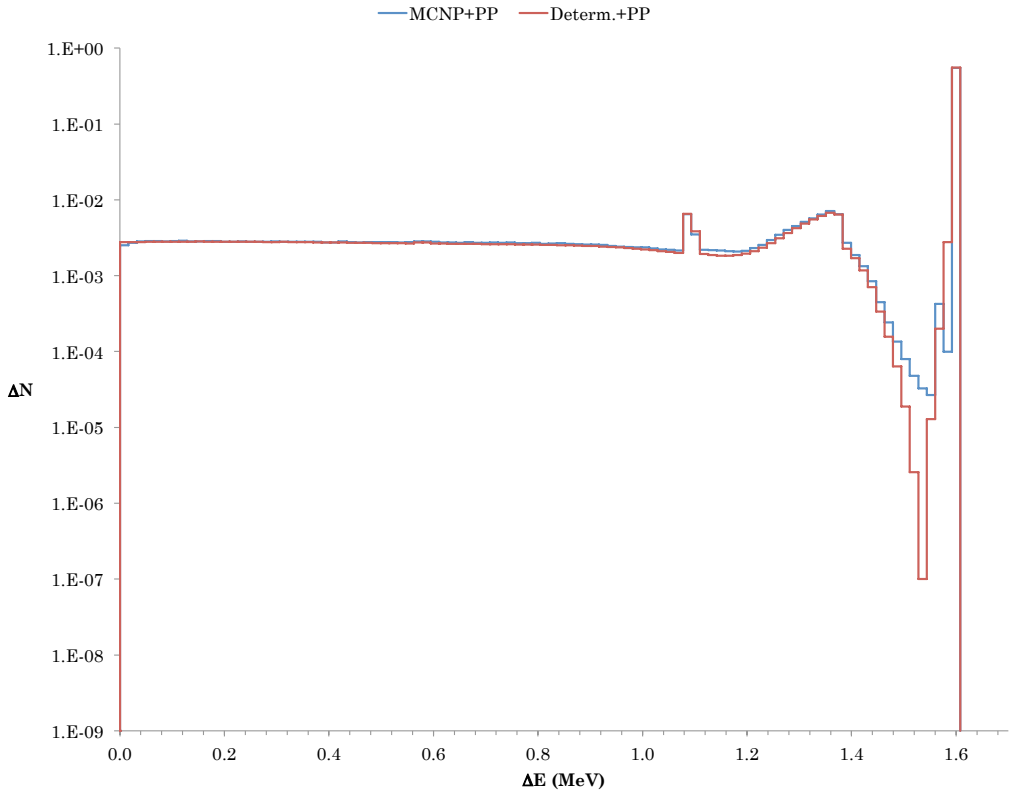

Figure 21: Pulse height distributions from 1.6 MeV photons normally ($\mu = 0.997$) incident on a 10 cm thick sodium iodide slab using the OOC pair production treatment and MCNP5. ρ=3.67 g/cm^3 (15 wt.% Na, 85 wt.% I)

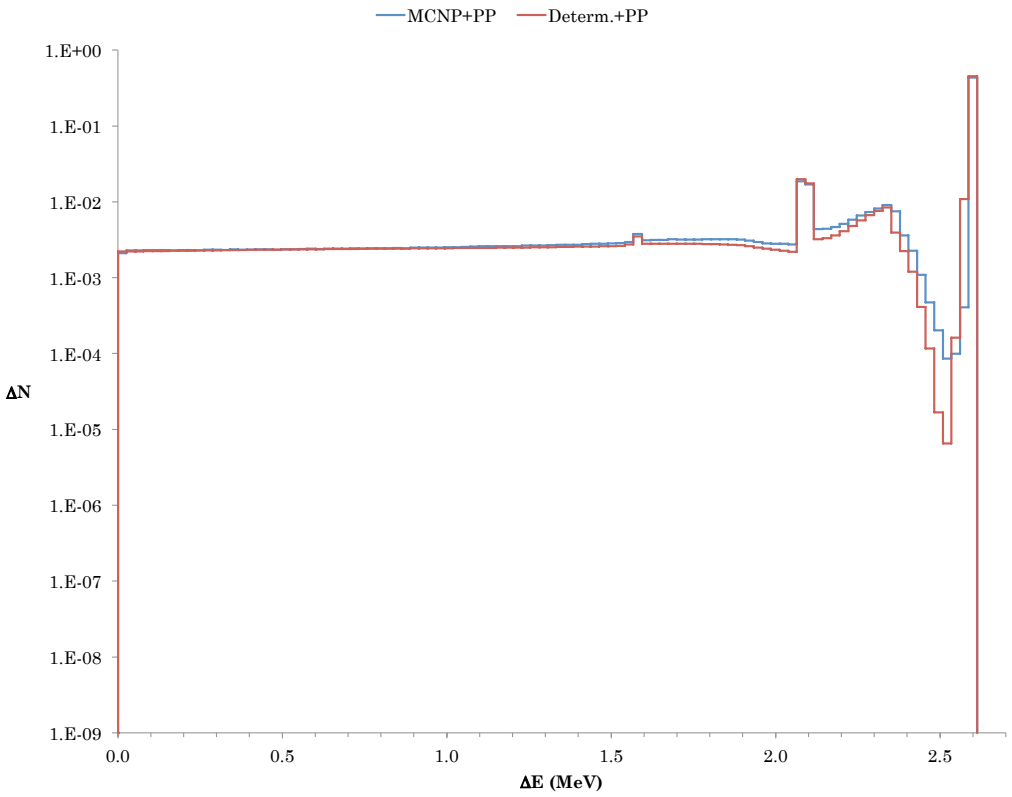

Figure 22: Pulse height distributions from 2.6 MeV photons normally ($\mu = 0.997$) incident on a 10 cm thick sodium iodide slab using the OOC pair production treatment and MCNP5. ρ=3.67 g/cm^3 (15 wt.% Na, 85 wt.% I)

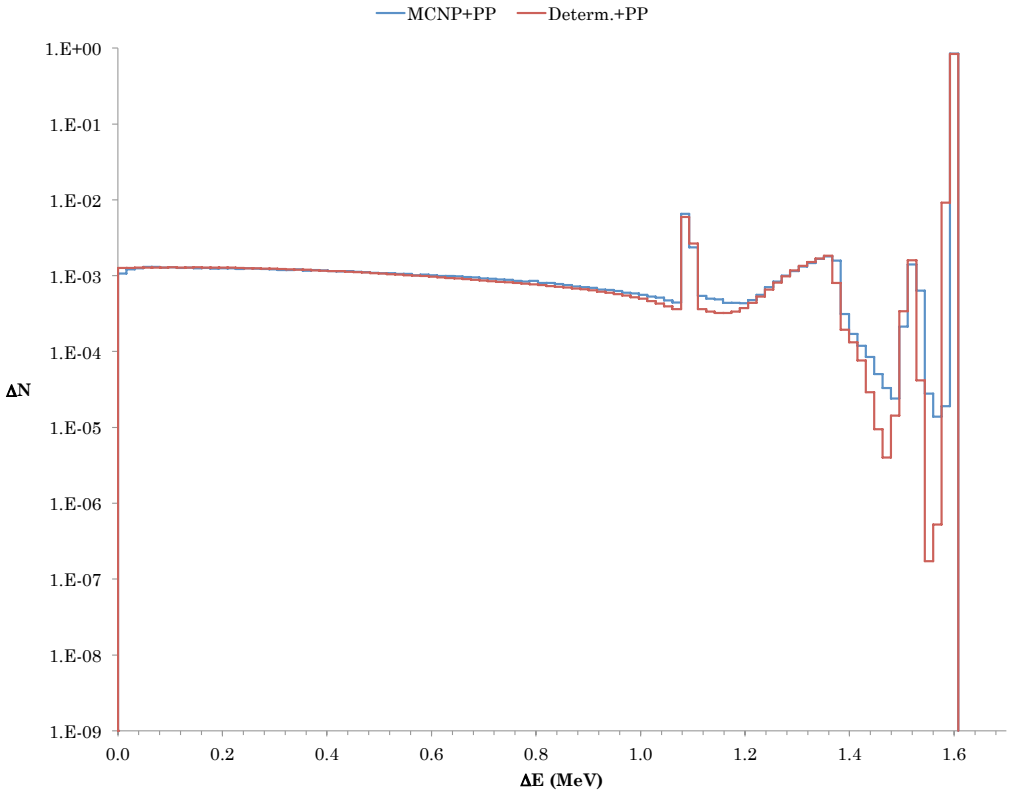

Figure 23: Pulse height distributions from 1.6 MeV photons normally ($\mu = 0.997$) incident on a 5 cm thick lead slab using the OOC pair production treatment and MCNP5. ρ=11.34 g/cm^3

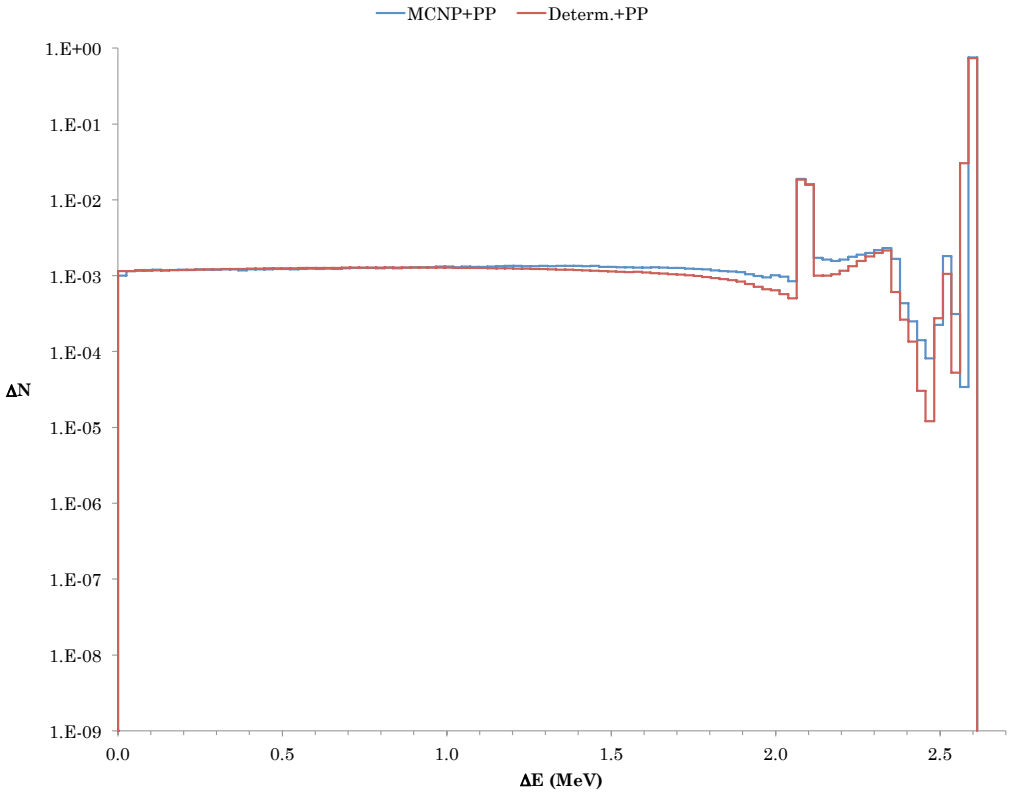

Figure 24: Pulse height distributions from 2.6 MeV photons normally ($\mu = 0.997$) incident on a 5 cm thick lead slab using the OOC pair production treatment and MCNP5. ρ=11.34 g/cm^3

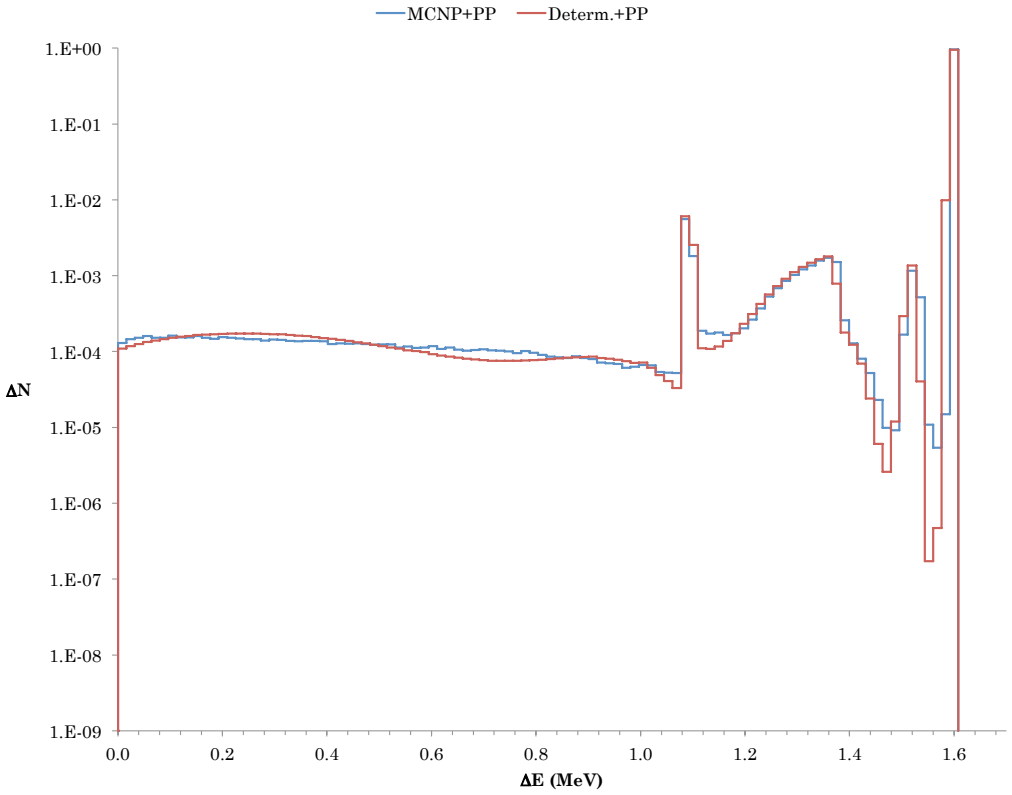

Figure 25: Pulse height distributions from 1.6 MeV photons normally ($\mu = 0.997$) incident on a 10 cm thick lead slab using the OOC pair production treatment and MCNP5. ρ=11.34 g/cm^3

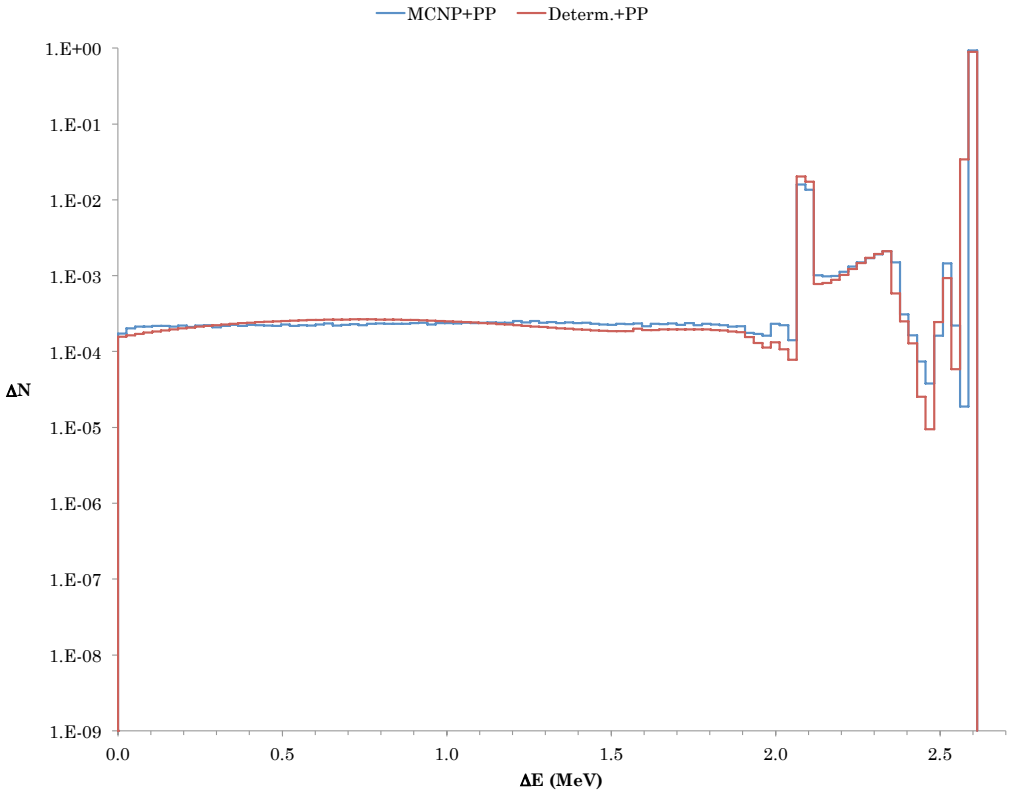

Figure 26: Pulse height distributions from 2.6 MeV photons normally ($\mu = 0.997$) incident on a 10 cm thick lead slab using the OOC pair production treatment and MCNP5. ρ=11.34 g/cm^3

PHD Peak Area Comparison for 1.6 MeV Photons								
Δz	**Mat.**	Method	**DE**	**rel. err.**	**SE**	**rel. err.**	**ZE**	**rel. err.**
10	Ge	Determ.	4.03E-03		7.60E-03		6.38E-01	
		Determ.*	2.00E-03		7.50E-03		6.37E-01	
		MCNP	4.11E-03	1.40E-02	7.19E-03	1.08E-02	6.32E-01	2.00E-04
		% Diff.	2.02		-5.76		-0.94	
		% Diff.*	51.39		-4.36		-0.88	
	NaI	Determ.	5.50E-03		1.04E-02		5.57E-01	
		Determ.*	2.70E-03		1.02E-02		5.58E-01	
		MCNP	5.67E-03	1.18E-02	9.97E-03	9.20E-03	5.47E-01	3.00E-04
		% Diff.	3.00		-4.09		-1.90	
		% Diff.*	52.34		-2.34		-2.06	
	Pb	Determ.	1.99E-04		8.61E-03		9.56E-01	
		Determ.*	9.95E-05		6.55E-03		9.67E-01	
		MCNP	2.25E-04	5.96E-02	7.41E-03	1.16E-02	9.67E-01	1.00E-04
		% Diff.	11.42		-16.18		1.08	
		% Diff.*	55.82		11.54		-0.08	
5	Ge	Determ.	6.91E-03		9.49E-03		3.27E-01	
		Determ.*	3.20E-03		1.03E-02		3.24E-01	
		MCNP	7.00E-03	1.06E-02	8.80E-03	9.60E-03	3.17E-01	5.00E-04
		% Diff.	1.35		-7.81		-3.08	
		% Diff.*	54.30		-17.03		-2.26	
	NaI	Determ.	7.05E-03		1.04E-02		2.81E-01	
		Determ.*	3.00E-03		1.22E-02		2.78E-01	
		MCNP	7.25E-03	1.04E-02	9.74E-03	9.30E-03	2.68E-01	5.00E-04
		% Diff.	2.70		-7.14		-4.80	
		% Diff.*	58.63		-25.20		-4.02	
	Pb	Determ.	1.99E-03		8.59E-03		8.39E-01	
		Determ.*	9.998E-04		7.86E-03		8.48E-01	
		MCNP	2.05E-03	1.97E-02	8.92E-03	1.04E-02	8.45E-01	1.00E-04
		% Diff.	2.85		3.62		0.67	
		% Diff.*	51.21		11.87		-0.38	

Table 4: Double (DE), single (SE), and zero (ZE) escape peak area comparisons for 1.6 MeV photons normally ($\mu = 0.997$) incident on 5 cm and 10 cm thick slabs of Ge, NaI, and Pb using the OOC pair production treatment. "Determ.*" and "% Diff.*" indicate results with no pair production treatment.

PHD Peak Estimate Comparison 2.6 MeV Photons								
Δz	**Mat.**	Method	**DE**	**rel. err.**	**SE**	**rel. err.**	**ZE**	**rel. err.**
10	Ge	Determ.	2.56E-03		2.76E-02		5.45E-01	
		Determ.*	2.30E-03		2.84E-02		5.38E-01	
		MCNP	2.66E-03	6.10E-03	2.57E-02	5.50E-03	5.29E-01	3.00E-04
		% Diff.	3.74		-7.60		-3.04	
		% Diff.*	13.64		-10.58		-1.80	
	NaI	Determ.	3.51E-03		3.73E-02		4.54E-01	
		Determ.*	2.70E-03		3.87E-02		4.53E-01	
		MCNP	3.75E-03	5.20E-03	3.57E-02	4.70E-03	4.36E-01	4.00E-04
		% Diff.	6.42		-4.43		-4.01	
		% Diff.*	28.05		-8.32		-3.90	
	Pb	Determ.	2.01E-04		3.75E-02		8.89E-01	
		Determ.*	1.84E-04		2.76E-02		9.30E-01	
		MCNP	2.35E-04	2.06E-02	2.94E-02	5.20E-03	9.28E-01	1.00E-04
		% Diff.	14.36		-27.44		4.23	
		% Diff.*	21.60		6.27		-0.17	
5	Ge	Determ.	5.14E-03		2.82E-02		2.54E-01	
		Determ.*	3.10E-03		3.46E-02		2.38E-01	
		MCNP	5.26E-03	4.40E-03	2.41E-02	5.70E-03	2.32E-01	6.00E-04
		% Diff.	2.19		-16.97		-9.86	
		% Diff.*	41.02		-43.42		-2.58	
	NaI	Determ.	6.78E-03		3.30E-02		2.10E-01	
		Determ.*	2.70E-03		4.31E-02		1.98E-01	
		MCNP	6.95E-03	3.80E-03	2.93E-02	5.20E-03	1.88E-01	7.00E-04
		% Diff.	2.46		-12.67		-11.75	
		% Diff.*	61.14		-47.20		-5.12	
	Pb	Determ.	1.12E-03		3.42E-02		7.38E-01	
		Determ.*	1.10E-03		3.25E-02		7.66E-01	
		MCNP	1.28E-03	8.80E-03	3.48E-02	4.80E-03	7.57E-01	2.00E-04
		% Diff.	12.46		1.83		2.51	
		% Diff.*	14.13		6.64		-1.11	

Table 5: Double (DE), single (SE), and zero (ZE) escape peak area comparisons for 2.6 MeV photons normally ($\mu = 0.997$) incident on 5 cm and 10 cm thick infinite slabs of Ge, NaI, and Pb using the OOC pair production treatment. "Determ.*" and "% Diff.*" indicate results with no pair production treatment.

3.5 Modified First-Flight Approximation

Figures 27-32 are the results of the modified first-flight (MFF) approximation PHD simulations. They are compared against MCNP5 PHDs with matching bin structure. These figures are included to provide a qualitative comparison of MFF results

with those generated by MCNP5. The deterministic and MCNP5 PHD curves are labeled "Determ.+PP" and "MCNP+PP" respectively with "+PP" indicating that the effects of pair production are included in the distributions. All deterministic transport calculations used the S_{32} angular quadrature, 5 uniform spatial cells, and 10 scattered components of the flux.

The same data is displayed in Table 6 on page 82, where values are given for area under the single, double and zero escape peaks and the percentage difference between the MFF and MCNP5 area estimates. The percent difference, labeled % Diff, is given by:

$$\%\text{Diff} = \frac{\text{MCNP5} - \text{Determ.}}{\text{MCNP5}}. \tag{92}$$

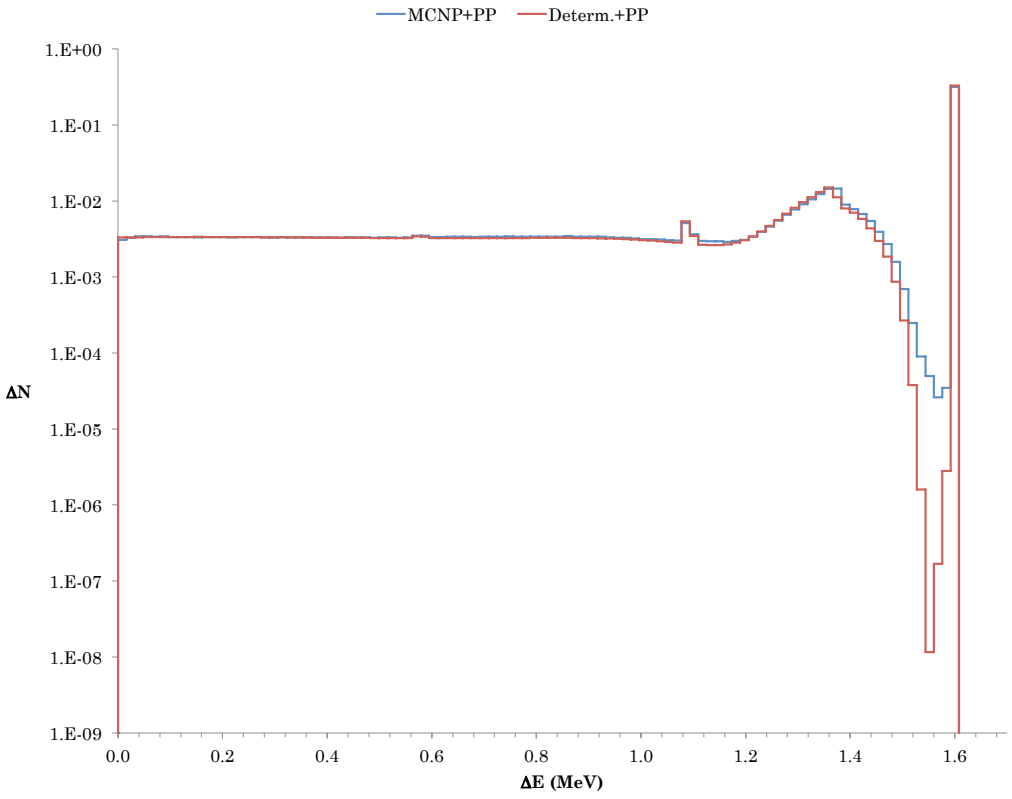

Figure 27: Pulse height distributions from 1.6 MeV photons normally ($\mu = 0.997$) incident on a 5 cm thick germanium slab using the first-flight pair production treatment and MCNP5. ρ=5.323 g/cm^3

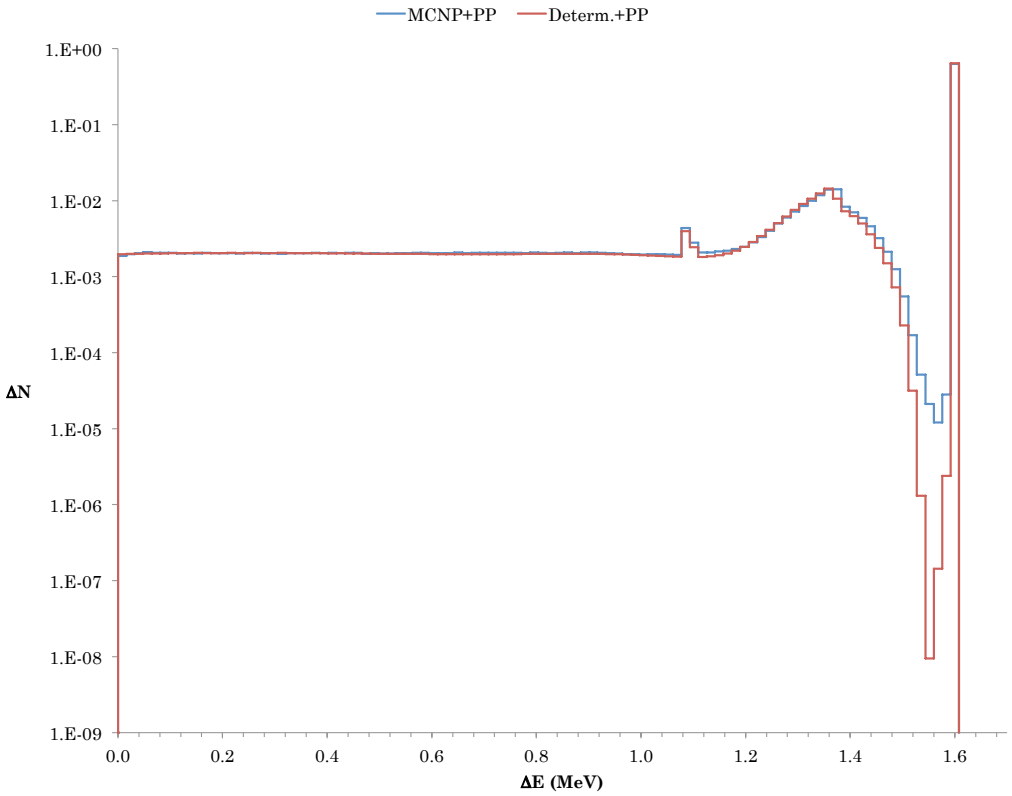

Figure 28: Pulse height distributions from 1.6 MeV photons normally ($\mu = 0.997$) incident on a 10 cm thick germanium slab using the first-flight pair production treatment and MCNP5. ρ=5.323 g/cm^3

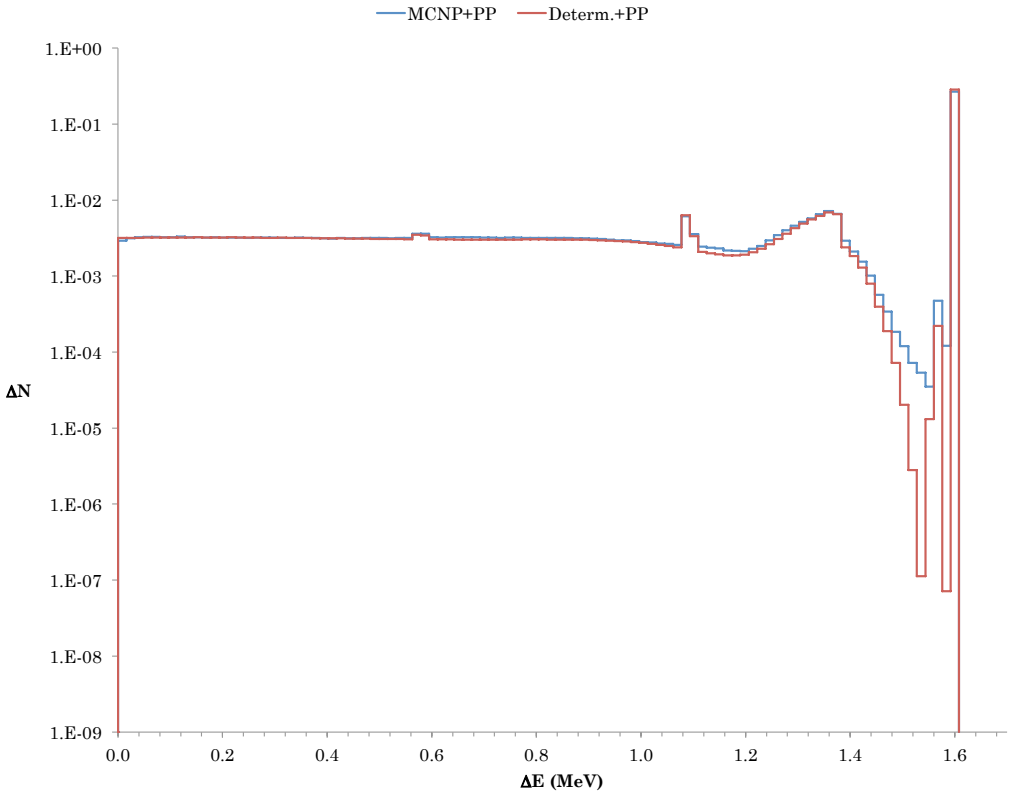

Figure 29: Pulse height distribution from 1.6 MeV photons normally ($\mu = 0.997$) incident on a 5 cm thick sodium iodide slab using the first-flight pair production treatment and MCNP5. ρ=3.67 g/cm^3 (15 wt.% Na, 85 wt.% I)

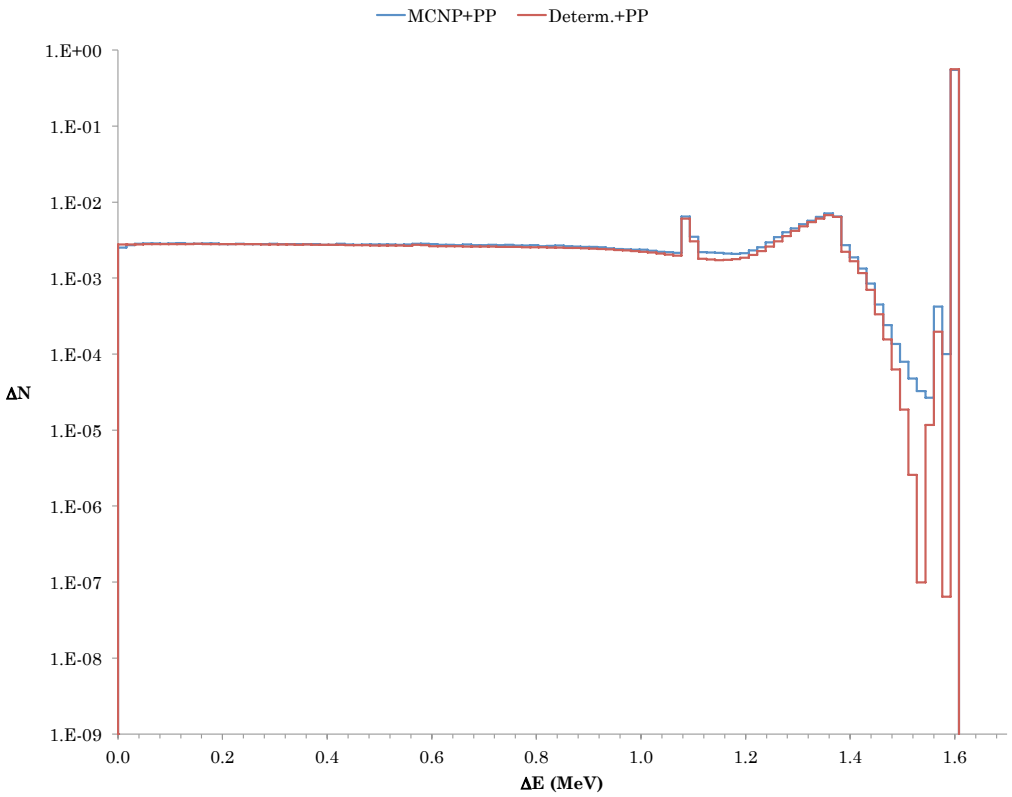

Figure 30: Pulse height distribution from 1.6 MeV photons normally ($\mu = 0.997$) incident on a 10 cm thick sodium iodide slab using the first-flight pair production treatment and MCNP5. ρ=3.67 g/cm^3 (15 wt.% Na, 85 wt.% I)

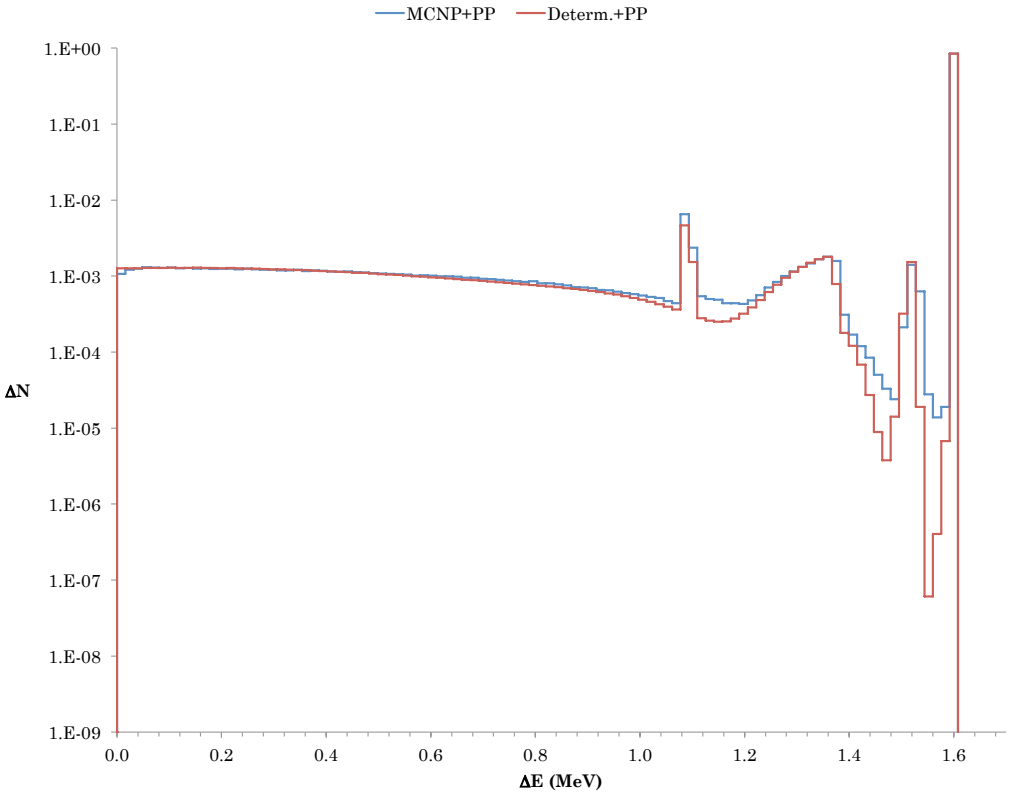

Figure 31: Pulse height distribution from 1.6 MeV photons normally ($\mu = 0.997$) incident on a 5 cm thick lead slab using the first-flight pair production treatment and MCNP5. ρ=11.34 g/cm^3

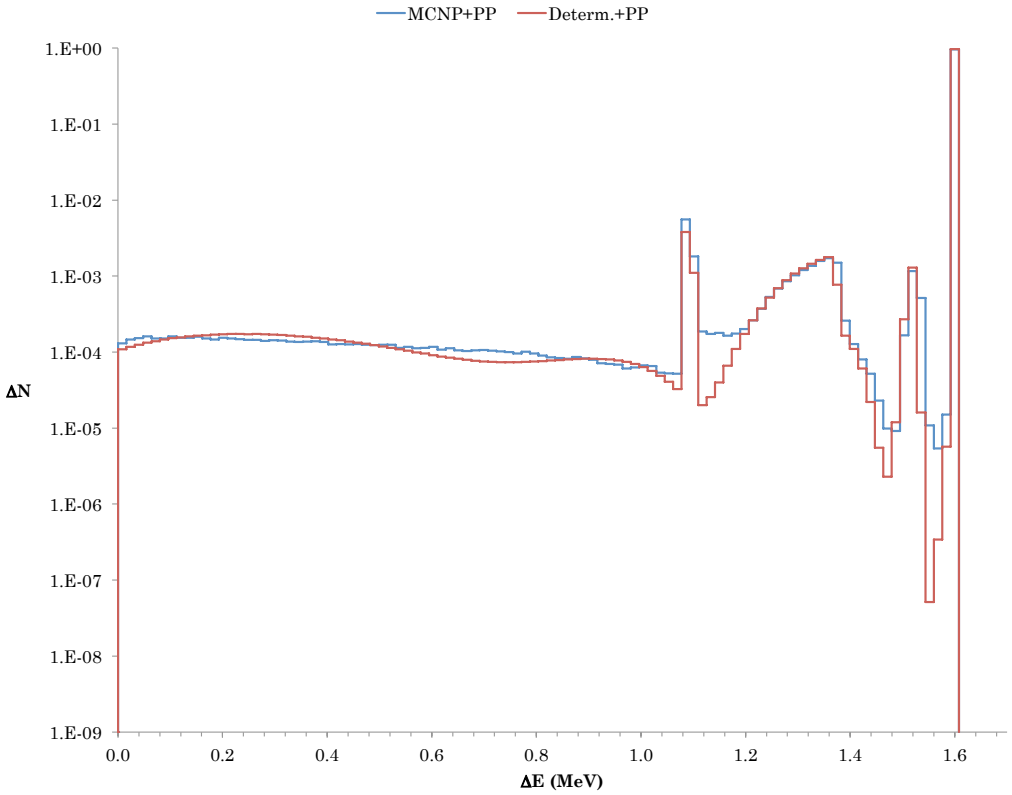

Figure 32: Pulse height distribution from 1.6 MeV photons normally ($\mu = 0.997$) incident on a 10 cm thick lead slab using the first-flight pair production treatment and MCNP5. ρ=11.34 g/cm^3

PHD Peak Estimate Comparison 1.6 MeV Photons								
Δ z	**Mat.**	Meth.	**DE**	**rel. err.**	**SE**	**rel. err.**	**ZE**	**rel. err.**
10	Ge	Determ.	4.02E-03		6.43E-03		6.42E-01	
		MCNP	4.11E-03	1.40E-02	7.19E-03	1.08E-02	6.32E-01	2.00E-04
		% Diff.	2.42		10.57		-1.71	
	NaI	Determ.	5.45E-03		9.14E-03		5.63E-01	
		MCNP	5.67E-03	1.18E-02	9.97E-03	9.20E-03	5.47E-01	3.00E-04
		% Diff.	3.81		8.25		-2.99	
	Pb	Determ.	1.95E-04		4.90E-03		9.71E-01	
		MCNP	2.25E-04	5.96E-02	7.41E-03	1.16E-02	9.67E-01	1.00E-04
		% Diff.	13.40		33.94		-0.42	
5	Ge	Determ.	6.82E-03		8.85E-03		3.30E-01	
		MCNP	7.00E-03	1.06E-02	8.80E-03	9.60E-03	3.17E-01	5.00E-04
		% Diff.	2.54		-0.51		-4.15	
	NaI	Determ.	6.92E-03		9.69E-03		2.84E-01	
		MCNP	7.25E-03	1.04E-02	9.74E-03	9.30E-03	2.68E-01	5.00E-04
		% Diff.	4.59		0.56		-6.21	
	Pb	Determ.	1.98E-03		6.17E-03		8.51E-01	
		MCNP	2.05E-03	1.97E-02	8.92E-03	1.04E-02	8.45E-01	1.00E-04
		% Diff.	3.01		30.76		-0.80	

Table 6: Double (DE), single (SE), and zero (ZE) escape peak area comparisons for 1.6 MeV photons normally ($\mu = 0.997$) incident on 5 cm and 10 cm thick slabs of Ge, NaI, and Pb using the first-flight pair production treatment.

3.6 Iteration Parameter Study Results

MCNP5 was used to investigate contributions to the total outgoing partal current j^+ from photons undergoing s collisions. The purpose of this investigation was to determine the number of scattered components (fixed source iterations) required for convergence. Five materials were chosen, spanning a wide range of charge density. For each material, slabs of thickness 1, 2, 4, 7, and 11 cm were modeled assuming a uniform distribution of 0.511 MeV photons (see Appendix C for MCNP5 input). Exiting partial current on each surface was tallied and the current tally was divided into bins of 0,1,2, ... 10 collisions occurring prior to the particle crossing the surface. The contribution from particles undergoing more than 10 collisions was determined using Equation 93.

$$j^{+s>10} = 1 + N_{Brem.} + N_{Fluor.} - \sum_{s=1}^{10} j^{+s} - N_{abs} \tag{93}$$

where N_{Brem} is the number of photons created due to bremsstrahlung, N_{Fluor} is the number of photons created through fluorescence, and N_{abs} is the total number of recorded photons absorbed.

The results of this study are shown graphically in Figures 33 - 38

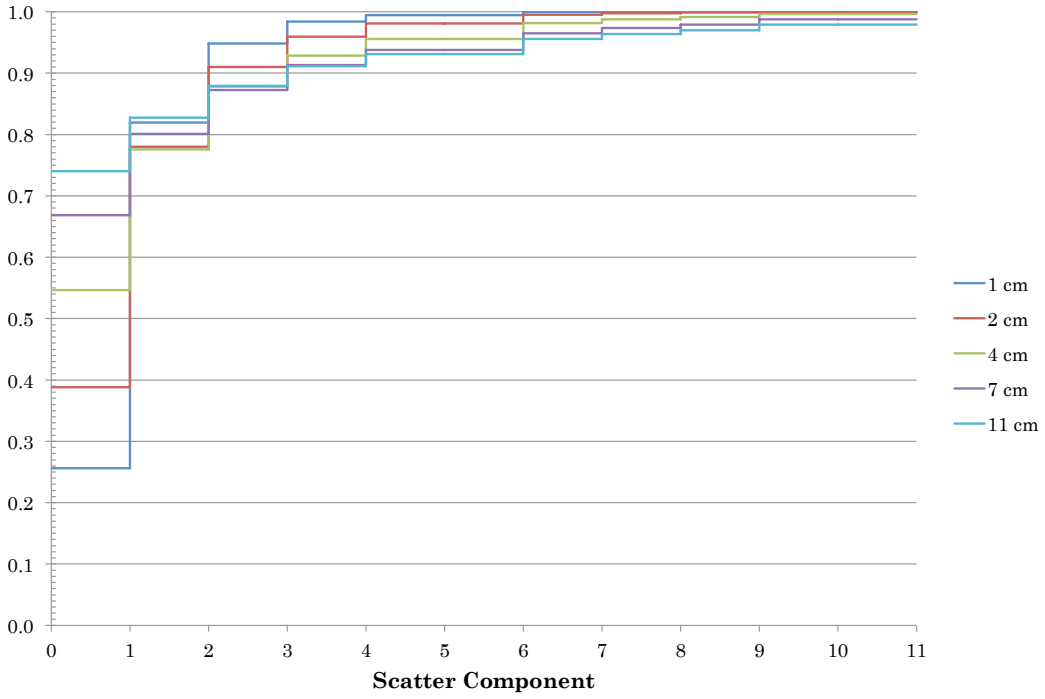

Figure 33: Percent of exiting partial current as a function of scattered flux components for carbon slabs of various thickness. ρ=2.267 g/cm^3

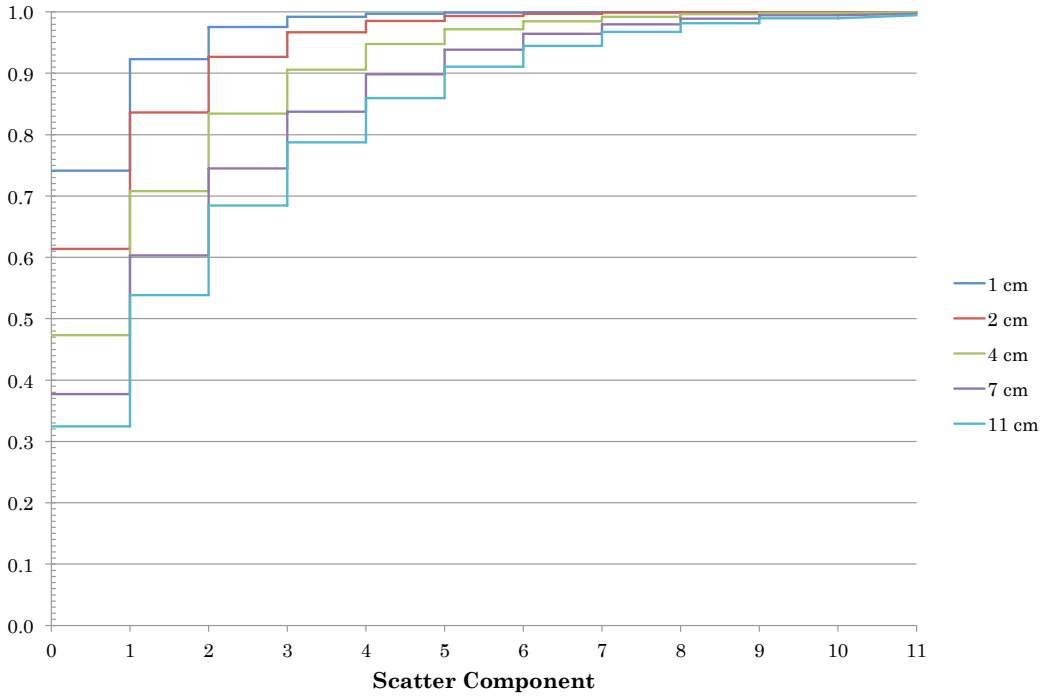

Figure 34: Percent of exiting partial current as a function of scattered flux components for silicon slabs of various thickness. ρ=2.329 g/cm^3

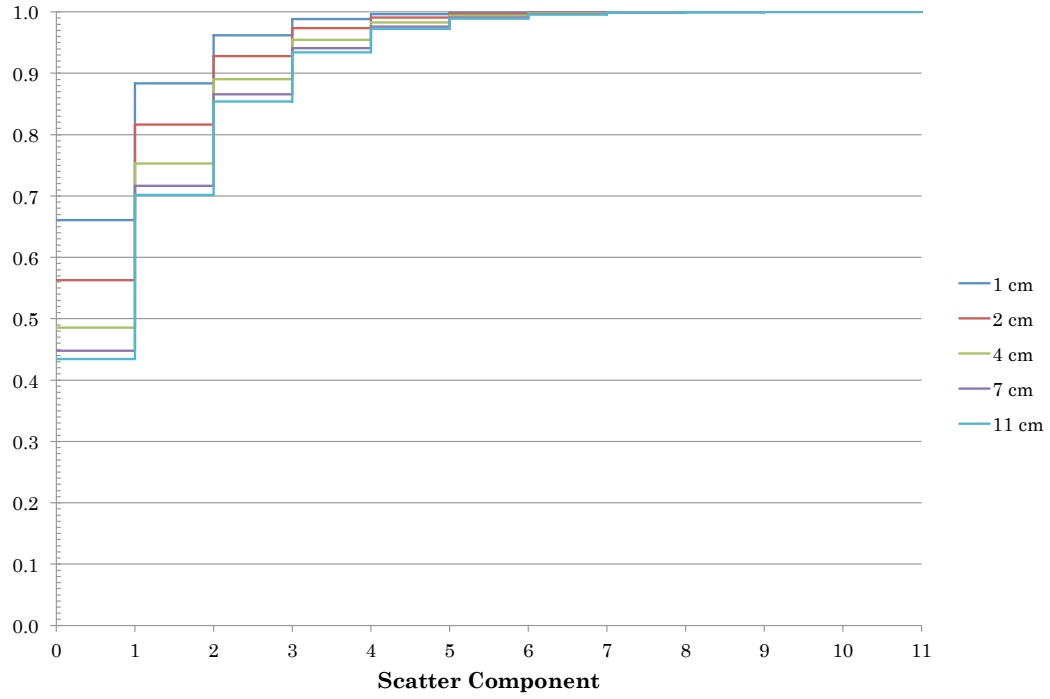

Figure 35: Percent of exiting partial current as a function of scattered flux components for germanium slabs of various thickness.. ρ=5.323 g/cm^3

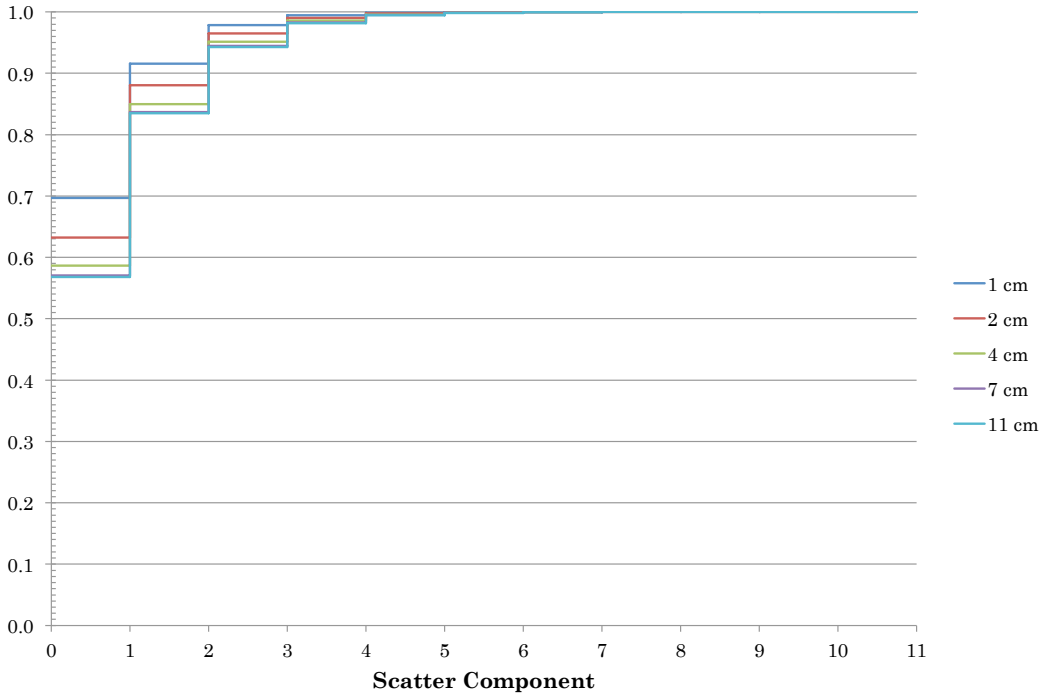

Figure 36: Percent of exiting partial current as a function of scattered flux components for tin slabs of various thickness. ρ=7.365 g/cm^3

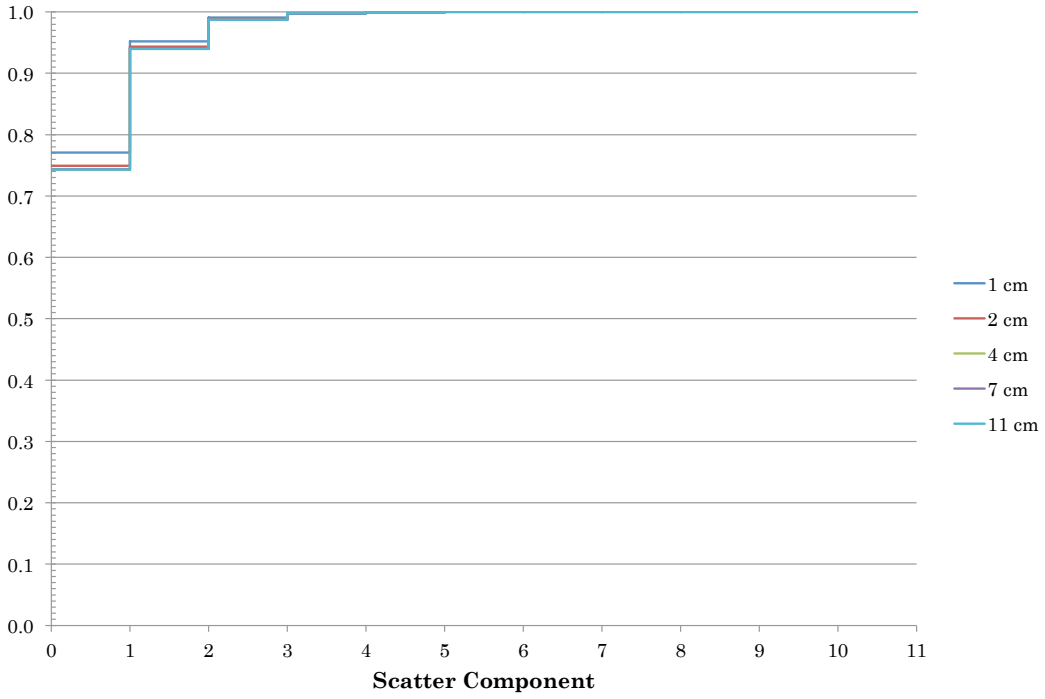

Figure 37: Percent of exiting partial current as a function of scattered flux components for lead slabs of various thickness.ρ=11.34 g/cm^3

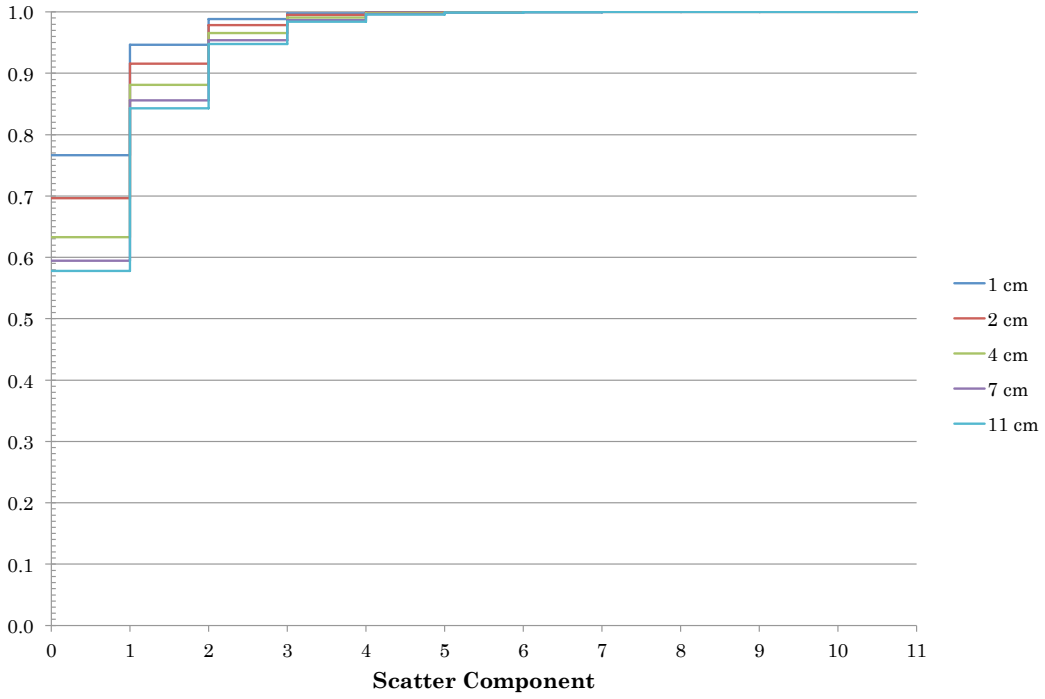

Figure 38: Percent of exiting partial current as a function of scattered flux components for sodium iodide slabs of various thickness. ρ=3.67 g/cm^3 (15 wt.% Na, 85 wt.% I)

4 Conclusions

4.1 Introduction

In this section, we begin with a discussion of the results of the energy deposition distributions proposed in Section 2.8 and then analyze the results from the opposing-ordinate combination and modified first-flight PHD methods. We then discuss the results of the iteration study and provide conclusions from our research and a discussion of possible future work.

4.2 Energy Deposition Distributions for Group-to-Group Transfer

Different approaches to treating the distribution of deposited energy resulting from within-group scatter and downscatter were presented in Section 2.8. The following subsections discuss the results of the within-group scatter and downscatter distributions, respectively.

4.2.1 Within-Group Scatter

The estimates for uncollided flux presented in Table 2 in Section 3.2.1 suggest that the distribution proposed for energy deposition resulting from within-group scatter in Section 2.8 is not inaccurate. Estimates are provided for several values of E^{ξ}_{cutoff}, which represents the upper bound of integration for Equation 85. This data is shown in Figures 39-41. In each of the three cases presented, the cutoff energy threshold required to match the MCNP5 estimate is nearly the full width of the first energy deposition bin. This indicates that the distribution of energy deposition for within-group scatter events should be much more heavily weighted

at zero. This finding is supported by the consistency of the MCNP5 estimate over a range of cutoff energies ranging from 10% to 90% of the bin width. This indicates that the vast majority of events in the MCNP5 simulation occurred between 0 and 10% of the bin width– presumably very near zero.

The treatment of within-group scatter events has not been clearly discussed in previous work. In light of the results found in this research, we suggest that all escaping current having undergone within-group scatter be treated as uncollided. This approach produced deterministic uncollided flux estimates with less than 1% deviation from MCNP simulation using 10^{-5} MeV as the upper bound of the epsilon bin. Treating all within-group-scattered escaping current as uncollided does erroneously shift some events from the first energy deposition bin into the uncollided tally. This result is a depression of the PHD in the first energy bin. This effect can be seen in Figures 8-10 in Section 3.2.2.

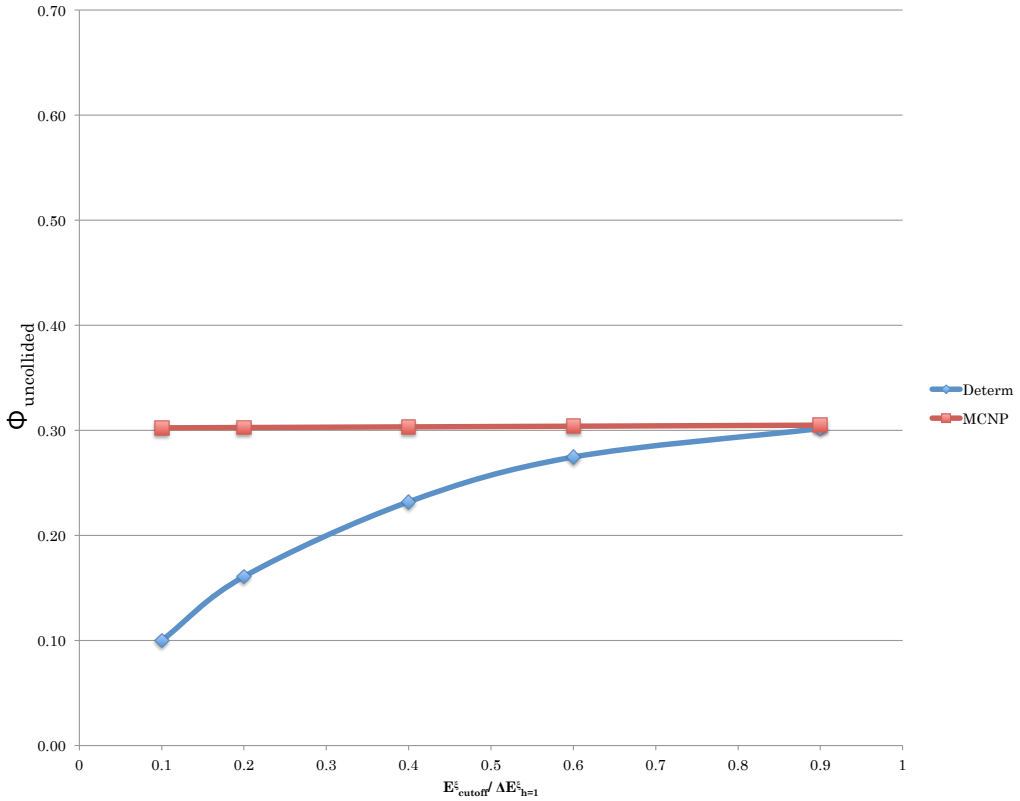

Figure 39: Uncollided flux estimates for 1.6 MeV photons normally ($\mu = 0.997$) incident on a 5 cm thick slab of germanium with a density of ρ=5.323 g/cm^3. In all cases S_{32} quadrature, 100 energy groups, and 1 cm cell thickness were used.

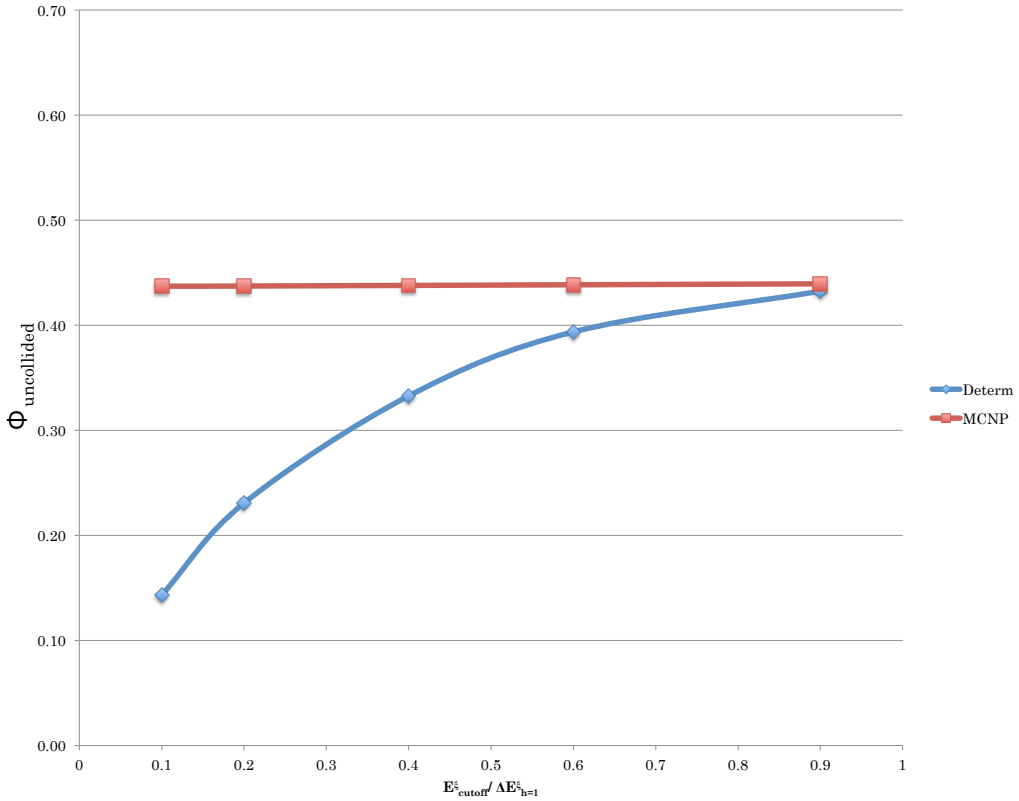

Figure 40: Uncollided flux estimates for 1.6 MeV photons normally ($\mu = 0.997$) incident on a 5 cm thick slab of sodium iodide with a density of ρ=3.67 g/cm^3 (15 wt.% Na, 85 wt.% I). S_{32} quadrature, 100 energy groups, and 1 cm cell thickness.

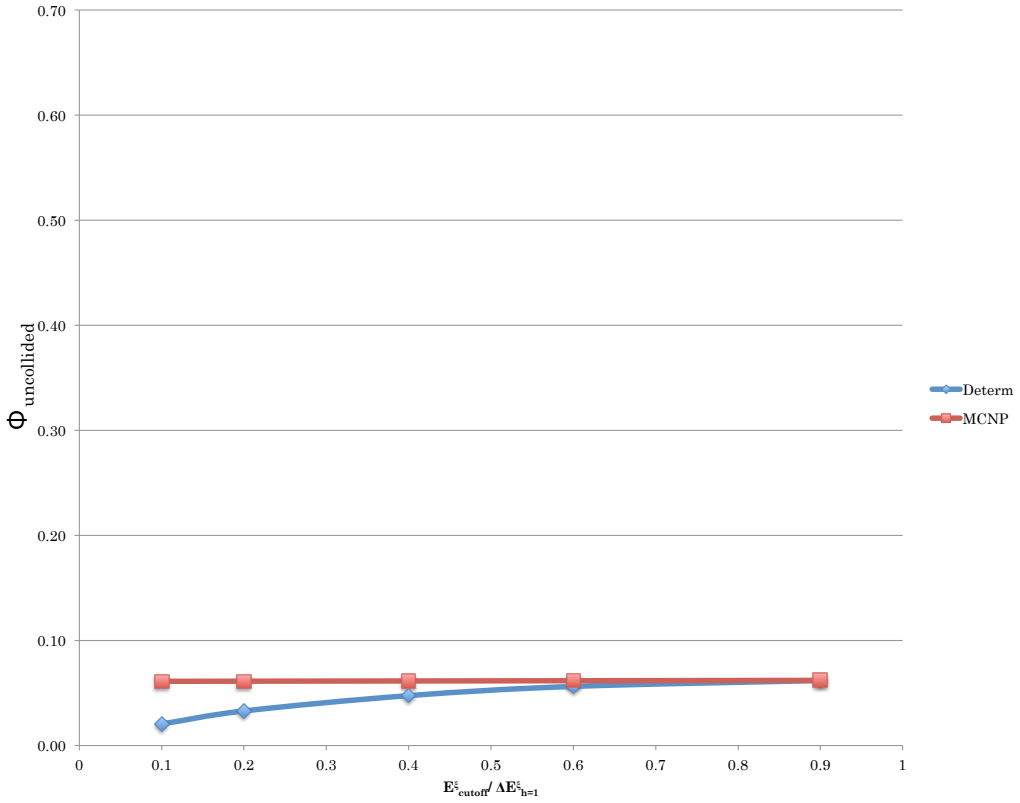

Figure 41: Uncollided flux estimates for 1.6 MeV photons normally ($\mu = 0.997$) incident on a 5 cm thick slab of lead with a density of ρ=11.34 g/cm^3. S_{32} quadrature, 100 energy groups, and 0.5 cm cell thickness.

4.2.2 Downscatter

Table 3 in Section 3.2.2 provides the average difference between deterministic and MCNP5 estimates of $\frac{\Delta N_h^\xi}{\Delta E_h^\xi}$ based on deposition energy distributions given by Equation 86 with the same energy deposition bounds. Reductions of 2.14%, 0.48%, and 1.47% were observed for the three cases presented. Bins in which the difference between the MCNP estimate and either of the deterministic estimates were greater than 200% were excluded. Bins with such error were observed in the region between the full-energy deposition peak and the Compton edge. Large errors in

this region have been observed in previous work and were attributed to differences in the multigroup and continuous cross section treatments [1]. The magnitude of those errors was extremely large relative to that of the other bins and made the comparison of the small changes resulting from the modified energy deposition distribution difficult to quantify.

The results indicate a slight advantage to using the triangular energy deposition distribution of Equation 86. The difference is not large and may not be worth expending extra effort to implement.

4.3 Separation of Annihilation Photons From Transfer Cross Sections

Because a method to explicitly isolate the production of annihilation photons from downscatter cross sections was not found, the pair production cross sections were taken to be the difference between aggregate transfer from energy groups (g') above the pair production threshold to the group containing 511 keV (g^*), and the average value of the aggregate transfer cross sections to the energy bins ($g^* \pm 1$) adjacent to group g^*. Correspondingly, the downscatter cross section was taken to be the aggregate transfer from group g' to the group containing 511 keV (g^*), less the contribution of annihilation photon production. Equations 94 and 95 explicitly define the annihilation pair source term.

$$S_{PP,g',n,i} = \frac{\phi_{g',i} w_n}{4} (\overline{\sigma}_{g' \to g^*} - \sigma_{s,g' \to g^*}) \tag{94}$$

where $\overline{\sigma}$ is the aggregate transfer cross section and $\sigma_{s,g' \to g^*}$ is given by:

$$\sigma_{s,g' \to g^*} = \frac{\overline{\sigma}_{g' \to g^*+1} + \overline{\sigma}_{g' \to g^*-1}}{2} \tag{95}$$

Figure 11 shows the annihilation photon production cross section (seen in orange). The smoothness of the trend in downscatter cross sections in the adjacent

groups supports the approach taken to isolate annihilation photon production. PHDs created from the transport solutions calculated using the scatter cross section defined by Equation 95 are shown in Figures 12-14 where they are compared to MCNP5 simulations. In all simulations performed, loss to pair production is treated as full absorption. The deterministic distributions exhibit no discontinuity in the flux for bins corresponding to g^* [1.08MeV, 1.10MeV] and have deviations from MCNP5 estimates of 1.87%, 1.90%, 3.05%, respectively. These results support the method used in this thesis to generate the "primary" PHDs.

4.4 Opposing-Ordinate Combination Method

Figures 15-26 show distributions created using the opposing-ordinate combination of full transport solutions. These distributions show good agreement with MCNP5 simulation throughout the Compton continuum and in the double escape, single escape, and full energy deposition peaks with average relative errors in those peaks being 3.9%, 7.4% and 2.1% for the 1.6 MeV source and 6.9%, 11.8% and 5.9% for the 2.6 MeV sources. The accuracy of the results from both 1.6 MeV and 2.6 MeV photon sources in the same material and geometric configuration supports the assertion that the system-specific effective annihilation photon PHDs (511-Pair PHDs) introduced in Section 2.2.2 only need to be generated once for a given system and can be used for any source.

Errors in the peak estimates for the 2.6 MeV source are approximately twice that seen in estimates based on a 1.6 MeV source. This difference is the result of the energy bin structure used to calculated the multi-group cross sections. Both problems used 100 groups– resulting in half the energy resolution in the 2.6 MeV source problems.

While peak estimates were accurate in most cases with little discernible trend in error, the largest discrepancies were observed in double escape peaks, and the error increased with increasing optical thickness. This may be due to increased uncertainty in the MCNP5 estimates and/or larger errors in the deterministic transport caused by increases in non-linearity of the scatter-source distribution within the cells. Negative flux solutions were observed in the lead problems with 1 cm spatial cells. Using higher spatial resolution or a negative flux fix-up may improve the results for this problem.

The disagreement between the Compton edge and full energy peak observed in previous works remains. The disagreement is exaggerated by the logarithmic scaling and is in a region of little practical importance to PHDs.

4.5 Modified First-Flight Approximation

Figures 27-32 show distributions created using the modified first-flight approximation. The distributions show strong agreement with MCNP5 simulations throughout the Compton continuum and in the double escape, single escape, and full energy deposition peaks. The relative error in area estimates of those peaks are 5.0%, 14.1%, and 2.7% respectively. As was the case in the opposing ordinate combination results, the lead systems have increased error in the peak estimates. The error may be some combination of error in the annihilation source distribution and error in the assumption that the scattered source distribution is spatially uniform following the first collision. Double escape estimates are near those predicted with OOC. This is expected because they are dependent only on uncollided ($s = 0$) photons. No approximation is made in the MMF method to treat these photons. PHDs were not generated for a 2.6 MeV source using the modified first-flight method.

The only difference between a 1.6 MeV source and a 2.6 MeV source would be the shape and magnitude of the annihilation photon distribution. Because a more penetrative 2.6 MeV source would produce a flatter annihilation photon source distribution, the results from this higher energy source would be likely be inside the error envelope produced by the 1.6 MeV source.

4.6 Iteration Parameter Study

The results of the iteration parameter study demonstrate that fewer iterations are needed for convergence than have been used in previous work. [Benz and Palmer[1] used 20 iterations in their research.] To achieve convergence accounting for 95% of the outgoing partial current, seven or fewer iterations are sufficient for the wide range of systems examined in Figures 33-38. These results can be used to guide the determination of the required number of scattered components to avoid wasted computing time. MCNP5 was used for this investigation for its established validity and because the code includes options which make this calculation easy to perform. Tally options used for the MCNP5 calculation can be found in Appendix C.

4.7 Comparison with Previous Work

Comparison of double, single, and zero escape peak estimates calculated using the OOC and MFF methods with those made using no pair production treatment shows a marked improvement. Without pair production treatment, deposition of energy from annihilation photons does not contribute to the double escape peak estimate. The error in estimates of that peak grows in proportion to the magnitude of the pair production source in the problem.

Quantification of error in the single escape peak estimate is somewhat difficult and misleading. As discussed in Section 1.8.3, when no pair production treatment is used, pair production results in the creation of two, independent 0.511 MeV photons which are sourced into the problem via the transfer cross sections. Essentially, they are treated as scatter from the incident energy group. The effect on the resulting PHD is the tally of all "true" events in which a 0.511 MeV photon escapes uncollided (e.g. double escape, single escape, or cases where one photon escapes uncollided and the other deposits some amount of energy $0< E^{\xi} < 0.511$ MeV) in the bin which corresponds to single escape. That is, without correction, a true double escape event would result in an increment of two in the SE bin, all true events where one photon escapes uncollided and the other deposits some amount of energy $0< E^{\xi} < 0.511$ MeV result in an increment of 1 in the SE bin, and true single escape events result in an increment of 1 in the SE bin. Of course, only the last event *should* contribute to the SE bin. The error in the SE bin is therefore dependent on the extent to which annihilation pairs are truly likely to undergo single escape events. This error is a complicated function of the system parameters (geometry, source definition, material properties).

In the test problems presented in this thesis, the error in the SE bins ranged from 47.20% to 2.34% without pair production treatment with corresponding OOC errors of 12.67% and 4.09%. Error values for all test problems, with and without pair production treatment, can be found in Tables 4 and 5 on pages 74 and 75. Again, these comparisons should be treated with caution due to the inconclusive nature of the SE bin tally in PHD where no pair production treatment is present.

4.8 Conclusions and Future Work

Both the opposing ordinate combination and the modified first-flight approaches produced accurate estimates of contributions to PHD peaks resulting for the production of annihilation photons. In the simple slab geometry systems examined in this thesis, the modified first-flight approach produces results with the same order of accuracy as estimates based on full linear characteristic transport. Because of the considerable time required to converge transport solutions for each combination of cell and ordinate (approximately 380 seconds per combination on a 2.4 GHz Intel Core 2 Duo using 2 GB of 1067 MHz DDR3 memory), the modified first-flight approach is preferred over the opposing ordinate combination approach.

In more complex systems where uniform spatial distributions of scattered annihilation photons may not be present(e.g. highly optically thick systems, complex geometries, inhomogeneous compositions, etc.) the full transport approach may be necessary. In that case the considerable computing required to run OOC would be an up-front cost which would produce a data set valid for any other analysis of the system– barring any changes to geometry or composition.

Future work may include developing a method to transport source photons in each ordinate and cell simultaneously while tracking fractions of $j+$ originating at each cell and ordinate. This is analogous to the approach taken by Benz and Palmer [1] to track fractions of j^+ originating at source energies. If such a method existed, the required computation would be reduced by a factor of $N * I$ where N and I are the angular quadrature and number of spatial cells respectively.

In the modified first-flight approximation, it may also be worthwhile to investigate estimates of the scattered source distributions which are more accurate in optically thick systems. These distributions may take on a form that relaxes toward

a uniform distribution after a sufficiently large number of scattering interactions. In both the OOC or MFF approaches, employing better spatial resolution may result in more accurate primary PHD and annihilation source distributions [12].

Bibliography

[1] Jacob Benz, Todd S. Palmer, *Pulse height distributions from deterministic radiation transport simulations* Annals of Nuclear Energy, Volume 37, Issue 11, p.1486-93, 2010

[2] J. Kenneth Shultis, Richard E. Faw, *Radiation Shielding* American Nuclear Society, Inc., Illinois Revised Edition, 2000

[3] Glenn F. Knoll *Radiation Detection and Measurement* John Wiley & Sons, Inc., 3rd Edition, 2000.

[4] George I. Bell, Samuel Glasstone, *Nuclear Reactor Theory* Van Nostrand Reinhold Company, New York, 1st Edition, 1970

[5] R. Douglas O'Dell, Raymond E. Alcouffe, *Transport Calculations for Nuclear Analyses* LA-10983-MS, Los Alamos National Laboratory, New Mexico 1987

[6] James J. Duderstadt, Louis J. Hamilton, *Nuclear Reactor Analysis* John Wiley & Sons, 1st Edition, 1976

[7] Marvin L. Adams, *Characteristic Methods in Thick Diffusive Problems* Nuclear Science and Engineering, Volume 130, p.18-46, 1998

[8] Brian C. Franke, Ronald P. Kensek, and Thomas W. Laub, *ITS Version 5.0: The Integrated TIGER Series of Coupled Electron/Photon Monte Carlo Transport Codes with CAD Geometry Revision 1* SAND2004-5172 Sandia National Laboratories, New Mexico 2005

[9] X-5 Monte Carlo Team, *MCNP A General Monte Carlo N-Particle Transport Code, Version 5 Volume 1: Overview and Theory* LA-UR-03-1987 Los Alamos National Laboratory, New Mexico 2003

[10] Harold Elford Johns, John Robert Cunningham, *The Physics of Radiology* Charles C Thomas - Publisher 4th Edition, 1983

[11] E.E. Lewis, W.F. Miller, Jr., *Computational Methods of Neutron Transport* American Nuclear Society 1st Edition, 1993

[12] Glenn E. Sjoden, *Exponential Characteristic Spatial Quadrature for Discrete Ordinates Neutral Particle Transport in Slab Geometry* Air Force Institute of Technology, 1992

Appendices

A Sample CEPXS Input

```
P 14 NaI rho=3.7g/cm3 100Grp Src=1.6MeV
CUTOFF 0.001
ENERGY 1.6
LEGENDRE 14
PHOTONS
LINEAR 100
PHOTON-SOURCE
NO-COUPLING
MATERIAL NA 0.1533 I 0.8467
DENSITY 3.7
PRINT
LEGENDRE 14
PRINT-ALL
```

B MCNP Pair Production Removal

```
PHD Benchmark, 1-D NaI 5cm No Pair Production
    1     1   -3.67  -2  1 -4 imp:p=1 imp:e=1
    2     0           3 -1 -4 imp:p=1 imp:e=1
    3     0          -3 :2 :4 imp:p=0 imp:e=0

    1     pz 0
    2     pz 5
    3     pz -0.5
   *4     cz 1000

mode  p e
m1    11000         -0.1533  $NaI
      53000         -0.8467
SDEF  POS = 0 0 0 AXS = 0 0 1
      ERG = D2 VEC = 0 0 1 DIR = D1
SI1 L 0.99726
SP1 1
SI2 H 1.592 1.608
SP2 D 0 1
PHYS:e 2 0 0 0 0 1 1 1 0 0
nps 10000000
F8:P 1
E8
      0.00000E+00
      1.00000E-09
      8.00000E-03
      2.40500E-02
      ..........
      ..........
```

C MCNP Scatter Order Tallying

```
PHD Benchmark, 1-D NaI
    1     1   -3.67  -2  1 -4 imp:p=1 imp:e=1
    2     0           3 -1 -4 imp:p=1 imp:e=1
    3     0          -3 :2 :4 imp:p=0 imp:e=0

    1        pz 0
    2        pz 5
    3        pz -0.5
   *4        cz 0.5

mode  p
m1    11000         -0.15  $NaI
      53000         -0.85
SDEF  POS= 0 0 0 AXS= 0 0 1 RAD= D1 EXT= D2
      ERG = 0.511
SI1 0 0.5
SP1 -21 1
SI2 0 5
SP2 0 1
nps 10000000
F4:P 1
FT4 INC
FU4 0 1 2 3 4 5 6 7 8 9 10
```